Materials Today Advances 25 (2025) 100549

Contents lists available at ScienceDirect

Materials Today Advances

journal homepage: www.journals.elsevier.com/materials-today-advances/

Segregation-guided alloy design via tailored solidification behavior

Ahmet Turnali [a,*], Dilay Kibaroglu [a], Nico Evers [b], Jaqueline Gehlmann [c], Lennart Sayk [b], Nicolas J. Peter [d], Abdelrahman Elsayed [e], Mehdi Noori [f], Tarek Allam [d], Johannes Henrich Schleifenbaum [b], Christian Haase [a,g]

[a] Chair Materials for Additive Manufacturing, TU Berlin, 10623, Berlin, Germany
[b] Digital Additive Production, RWTH Aachen University, 52072, Aachen, Germany
[c] Central Facility for Electron Microscopy, RWTH Aachen University, 52074, Aachen, Germany
[d] Institute of Energy Materials and Devices (IMD-1), Forschungszentrum Jülich GmbH, 52428, Jülich, Germany
[e] Steel Institute, RWTH Aachen University, 52072, Aachen, Germany
[f] Thermo-Calc Software AB, 16967, Solna, Sweden
[g] Center for 3D Technologies, TU Berlin, 10623, Berlin, Germany

ARTICLE INFO

Keywords:
Solidification
Segregation
Additive manufacturing
Microstructure
Multi-principal element alloy

ABSTRACT

This study presents an alloy design perspective guided by elemental segregation during solidification to determine the site-specific chemistry and related local thermodynamic properties of dendritic microstructures. This was accomplished via manipulation of the microsegregation behavior by means of nominal alloy composition and thermal conditions of the solidification processes, including modified cooling rates spanning over six orders of magnitudes using ingot casting, directed energy deposition (DED-LB/M) additive manufacturing (AM) and laser powder bed fusion (PBF-LB/M) AM processes. Our approach was demonstrated by computationally designing a novel $Al_xCo_{25}Fe_{(50-x)}Ni_{25}$ multi-principal element alloy (MPEA) as a model system, employing a combination of CALPHAD, Scheil, and multiphase-field simulations, and by experimentally validating the resulting microstructure evolution. The lower Al content ($x = 10.5$) was designated to generate a supersaturated single-phase fcc matrix suitable for heat-treatments to trigger local phase transformations. The higher Al content ($x = 14.5$) was selected to define the size and morphology of dual-phase microstructures by controlling phase nucleation and growth through segregation during solidification. Our results showcased how selective enrichment of the desired elements in interdendritic regions can be employed to induce local phase transformations during solidification or post heat-treatments, while their size can be flexibly controlled by the degree of undercooling during solidification. The suggested segregation-guided design approach can be transferred to other alloy systems, enabling effective tuning of local functional, structural, kinetic, and, as shown in this study, thermodynamic properties of dendritic microstructures by predetermining the nature of the alloy matrix through tailored solidification behavior.

1. Introduction

Segregation of alloying elements is an important metallurgical phenomenon within alloys, which manifests across various length scales. In the context of solidification, segregation arises from non-uniform distribution of alloying elements or impurities within the solidified material. Instances may include macroscopic centerline segregation established during solidification [1], covering distances comparable to the size of the casting. Another example is the localized enrichment of elements in the microscale between intra- and interdendritic regions (referred to as microsegregation) driven by constitutional undercooling [2], which occurs through the distances similar to the dendrite arm spacings. Additionally, the segregation of solute atoms can be promoted by appropriate post heat-treatments in micro- or nanoscale as a product of solid-state diffusion [3] to facilitate phase transformations through lattice defects, such as grain boundaries and dislocations [4].

In particular, controlling microsegregation behavior holds a significant relevance as it can be utilized for microstructure design [5–15]. It provides the possibility to modify the microstructure during solidification through solute partitioning between solid and liquid, enabling local

* Corresponding author.
E-mail address: turnali@tu-berlin.de (A. Turnali).

https://doi.org/10.1016/j.mtadv.2024.100549
Received 12 September 2024; Received in revised form 16 December 2024; Accepted 21 December 2024
Available online 31 December 2024

variations of composition, crystal structure and/or driving forces for phase transformation between intra- and interdendritic regions in the as-solidified microstructure. These variations can be carefully adjusted by changing thermal conditions during solidification and nominal alloy composition to dictate the site-specific structural and functional properties of metallic materials [7,12,16,17]. Nevertheless, understanding the interplay between alloy composition and segregation behavior in a wide range of thermal conditions during solidification plays a key role to exploit these possibilities. Various casting methods offer different thermal conditions; for instance, in melt spinning, cooling rates can reach up to 10^6 K/s [18]. However, precise control of the microstructure is uniquely achievable through additive manufacturing (AM) due to its layer-wise fabrication and the potential to adjust printing parameters in a flexible manner throughout the process [19]. In this regard, AM presents distinct opportunities to modify the microsegregation behavior [7], as it enables to print site-specific and scalable microstructures by exerting a significant control over the local cooling conditions [19,20]. For instance, cooling rates corresponding to the laser powder bed fusion (PBF-LB/M) process allow for the refinement of segregation into ultra-fine patterns, e.g., down to the nanometer scale [21]. Hence, this can reduce the size of the interdendritic regions and, if the alloy composition allows, the size of secondary phases formed in interdendritic regions. Moreover, unlike many casting methods, AM circumvents macrosegregation phenomenon, due to the high cooling rates and small melt pools inherent to AM processes.

Thus, through leveraging thermodynamics and solidification kinetics, the microsegregation behavior can be specifically modified both quantitatively and morphologically. These modifications can be attained by careful selection of alloying elements and processing parameters. The former can be used to manipulate the partitioning coefficients, e.g., compound forming elements can be selectively segregated to interdendritic regions, while the latter can determine the thermal conditions during solidification, governing diffusion distances and the degree of undercooling experienced by liquid at a given time [14]. Consequently, this dual control mechanism can effectively change the local chemistry and length scales of the intra- and interdendritic regions. This enables the segregation-guided engineering of specific regions within the microstructure that exhibit adjustable characteristics, such as their tendency to phase transformation [5,21]. Hence, the heterogeneous elemental distribution and respective length scales can also be used to predetermine the microstructure of the metal matrix, for instance, prior to the aging heat-treatment to induce site-specific precipitation, and the desired effects can therefore be enhanced.

Previously, several studies explored different approaches under the concept of segregation engineering, which predominantly involved altering the chemical or structural state of the grain boundaries via segregation. One subset of segregation engineering approaches provided pathways to mitigate the hot tearing behavior by controlling solute segregation through alloy composition, such as employing grain boundary strengthening additives [8], changing the content of compound forming alloying elements [9], and compositional modifications to promote liquid back-filling [6]. The other, and more traditional subset of segregation engineering approaches mainly incorporated heat-treatments to induce solute decoration of lattice defects, for instance, grain boundaries, to trigger phase transformations. The goal was to design microstructures that enhance the mechanical properties of complex alloys, especially when grain boundaries occupy a large portion of the microstructure [3,22]. In the current study, a key distinction is made by not focusing on using grain boundaries as the primary domain for designing microstructures. Instead, the "segregation-guided alloy design" approach puts emphasis on governing the characteristics of the alloy matrix by leveraging intrinsic segregation behavior during solidification to define its critical features. This is achieved by adjusting the length scales and local chemical characteristics of the alloy matrix, e.g., between intra- and interdendritic regions, by guiding the segregation behavior through nominal alloy composition and thermal conditions of the solidification processes. Therefore, our approach offers a microstructure design concept that can be achieved solely through solidification, for instance, without the need for thermomechanical treatments as in the traditional concept of segregation engineering.

The concept of segregation-guided alloy design can be exploited in highly alloyed systems [12,13], such as multi-principal element alloys (MPEAs), where the vast compositional space offers a large degree of freedom in their microstructure design and flexibility to activate multiple interconnected mechanisms between microstructure and final material properties [23–25]. The hypothesis suggests that in face-centered cubic (fcc) MPEAs, the increased stability of the body-centered cubic (bcc/B2) phases in both low and elevated temperature regimes can be provoked by a sufficient addition of Al [15,26,27]. Accordingly, the alloy design in this study was achieved through computational alloy selection employing thermodynamic calculations and Scheil solidification simulations. In this context, the novel Al_x-$Co_{25}Fe_{(50-x)}Ni_{25}$ MPEAs was selected as a model system from the Al-Co-Fe-Ni composition space, where the Al concentration was changed at the expense of Fe. This does not only make the alloy system eligible for the manipulation of the solidification sequence from primary fcc to primary bcc but also for heat-treatments to induce B2-precipitates over a wide range of temperatures, particularly towards lower Al contents. Thus, to demonstrate these phenomena, two compositions were utilized for investigation, namely, $Al_xCo_{25}Fe_{(50-x)}Ni_{25}$ with $x = 10.5$ and 14.5 at. %. The lower Al content was designated to generate a supersaturated single-phase fcc matrix for the design of a state suitable for aging heat-treatments to induce precipitation strengthening. The higher Al content was chosen to obtain dual-phase fcc-bcc microstructures in as-solidified state. Here, the dual-phase material is designed to introduce a network of the B2-phase according to size and morphology of the solidification structure, which holds relevance for high-temperature applications [28–32]. The calculations were complemented by multiphase-field simulations to unveil the potential for modifying the length-scales and morphologies of the elemental segregations as well as the fraction of B2-phase in as-solidified microstructures under different thermal conditions corresponding to ingot casting, directed energy deposition (DED-LB/M) additive manufacturing and laser powder bed fusion (PBF-LB/M) additive manufacturing. The specimens were fabricated by these processes and their microstructures were characterized experimentally by employing light optical microscopy (LOM), scanning electron microscopy (SEM), scanning transmission electron microscopy (STEM), electron backscatter diffraction (EBSD) and energy dispersive X-ray spectroscopy (EDS). Accordingly, the influence of the alloy composition and solidification conditions on segregation behavior and corresponding microstructure evolution was examined. Finally, the presented alloy design perspective and its utilization were experimentally demonstrated, with a critical discussion on its potential extension to other applications.

2. Computational methods

A combination of CALPHAD, Scheil and multiphase-field simulations were performed to understand the evolution of solidification microstructures of $Al_{10.5}Co_{25}Fe_{39.5}Ni_{25}$ and $Al_{14.5}Co_{25}Fe_{35.5}Ni_{25}$ alloys during ingot casting, DED-LB/M and PBF-LB/M processes.

Calculations of phase-equilibria and Scheil solidification simulations were performed using the software Thermo-Calc® [33] (2021b release, Thermo-Calc Software, Sweden) in combination with a custom thermodynamic database developed for multi-principal element alloys [34].

Microstructure-resolved simulations of phase and elemental distribution evolution were executed using the multiphase-field approach [35,36]. The simulations were conducted employing the phase-field solver MICRESS® (version 7.200, ACCESS e.V., Germany). The multiphase-field simulations were performed to examine the quantitative trends in microstructural features resulting from the influence of characteristic thermal conditions in a typical ingot casting, DED-LB/M

Table 1
Thermal conditions selected for multiphase-field simulations.

process	$\dot{T}$ [K/s]	G [K/cm]	R [cm/s]
Ingot casting	5	50	0.1
DED-LB/M	2.5×10^3	2.5×10^3	1
PBF-LB/M	10^6	10^5	10

and PBF-LB/M processes. The primary focus was on understanding the evolution of dendritic microstructures and B2-NiAl phase fractions based on specific solidification conditions. To this end, temperature gradients (G) and cooling rates ($\dot{T}$) were assumed to be constant and uniform with respect to space and time. This principle corresponds to the so-called frozen temperature approach, resulting in a steady-state solid-liquid interface velocity, i.e. solidification velocity, ($R = \dot{T}/G$) that was directed along the temperature gradient [37]. Consequently, in the present study, multiphase-field simulations modelled the solidification of the alloys in the region of the melt where G and $\dot{T}$ represented the specified thermal conditions for ingot casting, DED-LB/M, and PBF-LB/M processes. The range of G and $\dot{T}$ selected for the multiphase-field simulations were adopted from literature [38,39] and deliberately adjusted to achieve an increase in $\dot{T}$ by almost three orders of magnitude, G by almost two orders of magnitude and R by an order of magnitude between ingot casting, DED-LB/M and PBF-LB/M processes, respectively. The thermal conditions for multiphase field simulations are summarized in Table 1.

Multiphase-field simulations were performed in 2D with grid resolutions (Δx) of 1000, 100, and 10 nm for ingot casting, DED-LB/M and PBF-LB/M, respectively. A constant temperature gradient was uniformly applied in the Z direction, facilitating the movement of solid-liquid interface from bottom to the top of the simulation domain. The boundary conditions for the phase-field and concentration field were set to periodic from west to east and isolated at the bottom and top. For ingot casting simulations, the initial microstructure consisted of fcc and liquid phases, where the single fcc grain was set at the corner (coordinates of X = 0, Y = 0 and Z = 0) of the simulation domain. For DED-LB/M and PBF-LB/M simulations, an initial microstructure at t = 0 s was set as an almost flat fcc/liquid interface, where the single-phase fcc grain mimicked the previously deposited layer. This process facilitated the development of dendritic microstructures from planar front instability during both DED-LB/M and PBF-LB/M processes. Simultaneously, it assisted in obtaining comparable and representative microstructures suitable for primary dendrite arm spacing (PDAS) measurements. The nominal compositions of $Al_{10.5}Co_{25}Fe_{39.5}Ni_{25}$ and $Al_{14.5}Co_{25}Fe_{35.5}Ni_{25}$ alloys were considered as input compositions. During the multiphase-field simulations, random nucleation of B2-NiAl was allowed on the fcc/liquid interface, whereas random nucleation of the fcc phase was enabled on the B2-NiAl/liquid interface. The interfacial energies (σ) for solid-liquid and fcc/B2-NiAl interfaces were set to 2E-05 J/cm^2 [40] and 1.64E-5 J/cm^2, respectively. The stability of the nucleated seeds at the solid/liquid interface for the given temperature was calculated for each simulation time increment (for casting every 10^{-1} s, for DED-LB/M every 10^{-3} s, and for PBF-LB/M every 10^{-5} s). The maximum nucleation temperature for both fcc and B2-NiAl phase were selected as the liquidus temperature ($T_{Liquidus}$), namely 1684 K for the $Al_{10.5}Co_{25}Fe_{39.5}Ni_{25}$ alloy and 1652 K for the $Al_{14.5}Co_{25}Fe_{35.5}Ni_{25}$ alloy. Simulations stopped automatically once the liquid fraction was equal to zero. All simulations were integrated with thermodynamic and diffusion data obtained from a custom thermodynamic database developed for multi-principal element alloys [34] and MOBHEA2 mobility database from Thermo-Calc®, respectively, for realistic assessment of temperature-dependent thermodynamic driving forces and diffusion. To correct and alleviate the numerical trapping effects of the diffuse interface and to ensure diffusion-limited interface kinetics, redistribution of the elements at the solid-liquid interface was determined through the utilization of anti-trapping current [41] and automatic mobility correction embedded in MICRESS®.

Table 2
Chemical composition (at. %) of the bulk samples and powders measured by ICP-OES analysis.

states	Al (at. %)	Co (at. %)	Fe (at. %)	Ni (at. %)
Cast10.5	10.5	24.9	39.4	25.2
Cast14.5	14.2	25.3	35.4	25.1
DED10.5	10.3	24.0	40.3	25.4
DED14.5	14.0	26.0	35.0	25.0
PBF10.5	10.6	24.5	40.0	24.9
PBF14.5	14.5	25.0	35.0	25.5
$Al_{10.5}Co_{25}Fe_{39.5}Ni_{25}$ powder	10.8	24.7	39.1	25.4
$Al_{14.5}Co_{25}Fe_{35.5}Ni_{25}$ powder	14.6	26.0	33.6	25.8

3. Experimental methods

3.1. Materials and processing

The bulk samples for microstructure characterization were fabricated via ingot casting, DED-LB/M and PBF-LB/M with nominal compositions of $Al_{10.5}Co_{25}Fe_{39.5}Ni_{25}$ and $Al_{14.5}Co_{25}Fe_{35.5}Ni_{25}$.

The master ingots (18 kg) were ingot-casted under Argon (Ar) atmosphere by employing elemental flakes of Al, Co, Fe and Ni (each with > 99.8 % purity). Each master ingot was remelted 4 times to avoid macrosegregation. Samples with dimensions of 30 × 30 × 10 mm^3 were sectioned from the central region of the master ingots to characterize the as-solidified microstructures.

Gas-atomized elemental powders of Co, Fe, Ni (thyssenkrupp Raw Materials GmbH, Germany) and Al (TLS Technik GmbH, Germany) containing > 99.8 % purity and particle sizes ranging between 15 and 45 μm were blended using a tumbler mixer to achieve the specified nominal compositions. Powder blends were then utilized for the DED-LB/M process using a Lunovu MultiMAT DED-LB/M machine (LUNOVU GmbH, Germany) equipped with a Laserline LDF 6000-30 diode laser with a maximum laser power of 6 kW and a focus beam diameter of 1.5 mm. Powders were fed axially through a continuous coaxial nozzle using an Oerlikon Metco Twin 150 Powder Feeder (Oerlikon Metco AG, Wohlen, Switzerland) and deposited on a AISI 316L substrate. Ar (purity ≥ 99.996 %) with a flow rate of 10 L/min was used as a shielding and carrier gas. Bulk specimens with the dimensions of 60 × 10 × 10 mm^3 (transverse direction (TD), scanning direction (SD), building direction (BD)) were manufactured by employing a nominal laser power of 850 W, scan speed of 0.45 m/min and a powder feed rate of 2.2 g/min. A bi-directional build strategy without a rotation between subsequent layers was applied using a contouring path. The DED-LB/M samples were sectioned down to 30 × 10 × 10 mm^3 (SD, TD, BD) for subsequent microstructure characterization.

The custom atomized $Al_{10.5}Co_{25}Fe_{39.5}Ni_{25}$ and $Al_{14.5}Co_{25}Fe_{35.5}Ni_{25}$ powders were utilized for the PBF-LB/M process (Fig. S1). Bulk specimens with dimensions of 5 × 5 × 10 mm^3 (TD, SD, BD) with the particle size distribution ranging between 20 and 65 μm were fabricated using an Aconity-Mini PBF-LB/M machine (Aconity-3D GmbH, Herzogenrath, Germany) equipped with a Yb:YAG fiber laser (400W) with a Gaussian laser intensity profile and a focus diameter of 80 μm. The built chamber was purged with Ar (purity ≥ 99.996 %) with a flow rate of 1 L/min to reach a chamber pressure of 50 mbar and an average oxygen concentration below 1 ppm. A rotation of 90° between subsequent layers and a bi-directional scanning strategy were applied. For the $Al_{10.5}Co_{25}Fe_{39.5}Ni_{25}$ alloy, the PBF-LB/M process parameters of laser power, powder layer thickness, hatch spacing, and laser scan speed were selected as 200 W, 30 μm, 70 μm and 750 mm/s, respectively. For the $Al_{14.5}Co_{25}Fe_{35.5}Ni_{25}$ alloy, the PBF-LB/M process parameters of laser power, powder layer thickness, hatch spacing, and laser scan speed were employed as 200 W, 30 μm, 70 μm and 850 mm/s, respectively.

The selected DED-LB/M and PBF-LB/M parameters enabled the

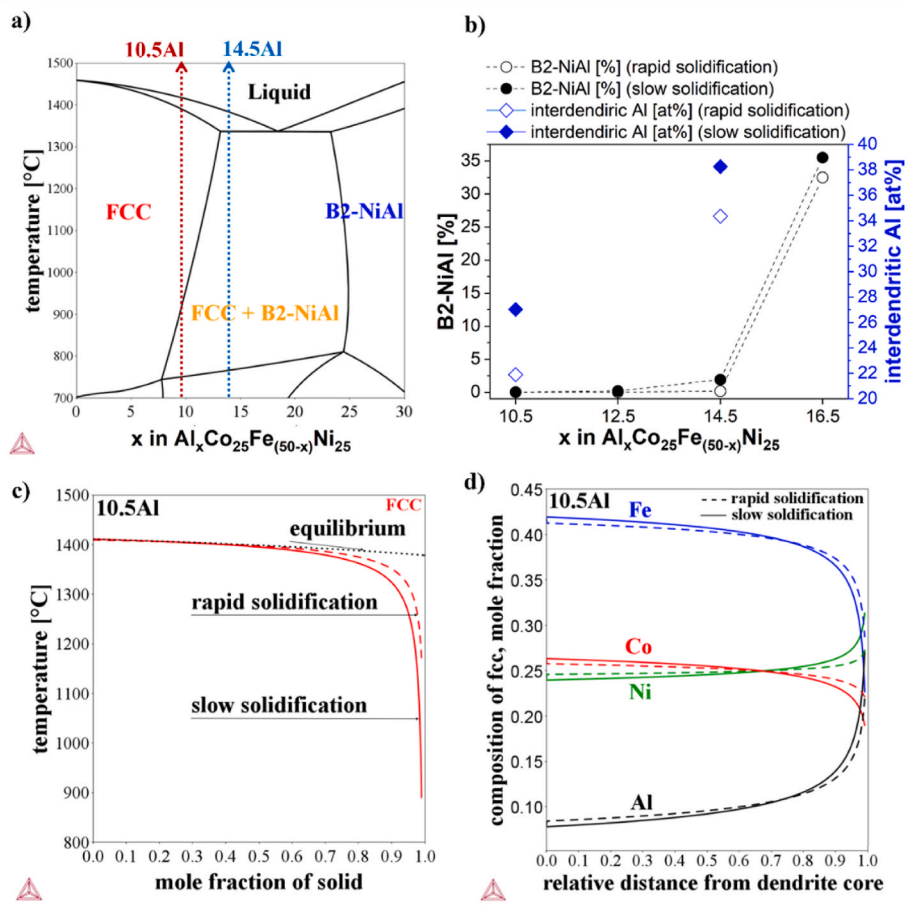

Fig. 1. (a) Equilibrium phase diagram of $Al_xCo_{25}Fe_{(50-x)}Ni_{25}$ with varying Al content. Red and blue dashed lines indicate 10.5 and 14.5 at. % Al, respectively. (b) Evolution of B2-NiAl phase fraction and interdendritic Al composition over a given range of nominal Al composition calculated by Scheil solidification simulations with solute trapping for $Al_xCo_{25}Fe_{(50-x)}Ni_{25}$ system. Scheil solidification simulations with solute trapping of (c) $Al_{10.5}Co_{25}Fe_{39.5}Ni_{25}$. The dashed lines represent rapid solidification conditions ($R = 1$ m/s), whereas straight lines demonstrate slow solidification conditions ($R = 0.001$ m/s). (d) Calculated composition profiles of fcc for $Al_{10.5}Co_{25}Fe_{39.5}Ni_{25}$. The distance in the x-axis shows the relative distance between the dendrite core (left side, first to solidify) and the middle of the interdendritic region (right side, last to solidify).

fabrication of dense bulk samples, achieving relative densities larger than 99.9 %, as determined through optical porosity measurements (Fig. S2). Micrographs for optical porosity measurements were captured using a Keyence VHX-6000 digital microscope (Keyence GmbH, Germany) and post-image processing was employed using the software ImageJ® [42]. In the following, the as-cast, as-DED-LB/M and as-PBF-LB/M samples with nominal compositions of $Al_{10.5}Co_{25}Fe_{39.5}Ni_{25}$ and $Al_{14.5}Co_{25}Fe_{35.5}Ni_{25}$ will be denoted as Cast#, DED# and PBF#, respectively, with # representing the Al content (10.5 and 14.5 at. %). The chemical compositions of bulk specimens manufactured by ingot casting, DED-LB/M and PBF-LB/M, as well as the compositions of pre-alloyed powders were determined via inductively coupled plasma optical emission spectrometry (ICP-OES) and are summarized in Table 2.

3.2. Microstructure characterization

Various microscopy techniques including light optical microscopy (LOM), scanning electron microscopy (SEM), electron backscatter diffraction (EBSD) and energy-dispersive X-ray spectroscopy (EDS), were employed to characterize the microstructures across different length scales. Sample preparation involved mechanical grinding up to 2500 SiC grit paper and mechanical polishing with 3 and 1 μm diamond suspension. Subsequent chemical surface treatments (e.g., etching) of the samples were tailored to suit the feature sizes (e.g., dendrite spacing, grain size, etc.) and corresponding microscopy techniques. Consequently, samples were color etched with Lichtenegger and Blöch (L-B) reagent for microstructure characterization via LOM. Electropolishing was performed at 22 V for 10 s at room temperature using a LectroPol-5 electrolytic polishing machine (Struers GmbH, Germany) and an A2 electrolyte (Struers GmbH, Germany) to facilitate microstructure characterization using SEM and EBSD.

SEM imaging, EDS and EBSD measurements were carried out on a Zeiss Sigma field emission gun (FEG) SEM with EDS and EBSD detectors (Oxford Instruments plc, Great Britain). SEM micrographs were acquired with backscattered electron (BSE) detector at an accelerating voltage of 10 kV with a working distance of 8 mm and an aperture size of 75 μm. EDS line scans were performed with an accelerating voltage of 15 kV at a working distance of 10 mm and a step size between 50 and 3000 nm. EBSD measurements were conducted with an accelerating voltage of 20 kV, a working distance between 14 and 16 mm and a step size varying between 80 and 2000 nm on a cubic grid. For EDS and EBSD measurements, step sizes were varied according to the process- and composition-specific feature size of the microstructures. Post-processing of the EBSD data was performed via the MATLAB®-based (Mathworks Inc., USA) toolbox MTEX [43–45].

Specimens for scanning transmission electron microscopy (STEM) were acquired using a Helios 5 (ThermoFisher Scientific) plasma focused ion beam (PFIB). Lamellae were extracted in cross-section parallel to the build direction (BD) and transferred to a STEM Cu grid using the common lift-out technique. The extracted lamellae were thinned to electron

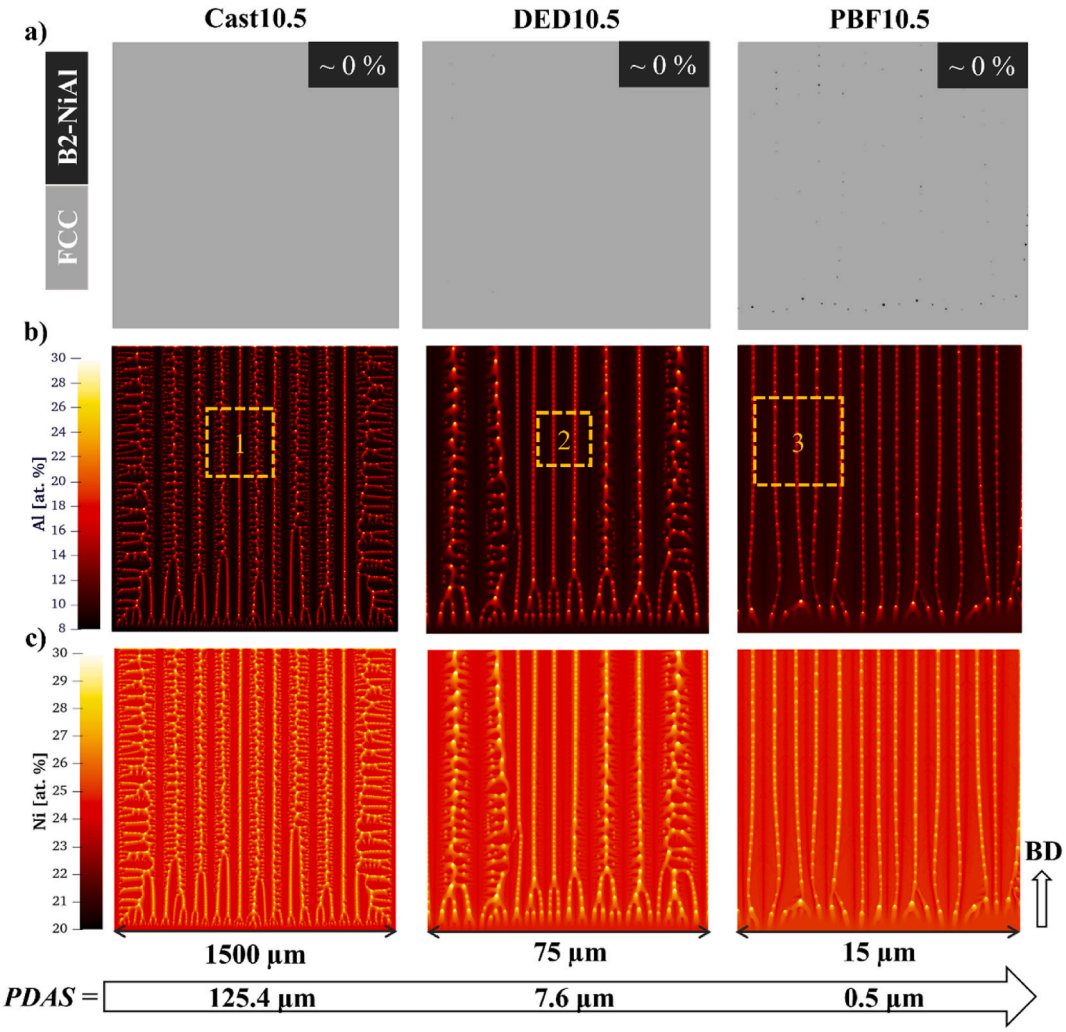

Fig. 2. Multiphase-field simulation results for the solidification of $Al_{10.5}Co_{25}Fe_{39.5}Ni_{25}$ alloy under thermal conditions resembling ingot casting, DED-LB/M and PBF-LB/M processes. BD shows the building direction for DED-LB/M and PBF-LB/M processes. (a) Phase maps, (b) Al and (c) Ni distributions maps. Orange dashed boxes indicate the close-ups sectioned for the virtual EDX line scans in Fig. 4a. PDAS measurements for each process were taken along the complete cross-section. The values in the black boxes represent the B2-NiAl area fraction as determined from multiphase-field simulations.

transparency with a final 5 kV ion polishing step to minimize damage. STEM imaging was performed at 200 kV with a 24.7 mrad semi-convergence angle on an aberration-corrected Titan G2 60–200 CREWLEY microscope, equipped with a high-brightness field emission gun and a Super-X EDS system. Bright field (BF) STEM images were acquired with a 19 mrad semi-collection angle range.

Synchrotron X-ray diffraction (SYXRD) measurements were conducted at the Deutsches Elektronen-Synchrotron (DESY) (Hamburg, Germany), using the PETRA III beamline, station P21.2. The samples were mechanically grinded to a thickness of approximately 1 mm before the measurements. The beamline operated at a fixed photon energy of 82.5 keV, corresponding to an X-ray wavelength of approximately 0.1503 Å. The beam spot size was 1 mm × 1 mm, and the diffraction patterns were obtained using Varex XRD 4343 C T detectors.

4. Results

4.1. Phase-equilibria and solidification simulations

Fig. 1a illustrates the calculated equilibrium phase diagram for Al_x-$Co_{25}Fe_{(50-x)}Ni_{25}$ MPEA with varying Al contents. Overall, an increase in Al content at the expense of Fe led to a transition from the fcc to the fcc-B2-NiAl phase field, and finally to the B2-NiAl phase field. The calculations predicted that the rise in Al content effectively stabilized B2-NiAl at elevated temperatures. Thus, based on the phase-equilibria demonstrated in Fig. 1a, the $Al_xCo_{25}Fe_{(50-x)}Ni_{25}$ system was suitable for the modification of the solidification mode from single-phase fcc to dual-phase fcc-B2-NiAl by increasing the Al content.

While the phase diagram is based on equilibrium calculations, Scheil solidification simulations enable the prediction of microsegregation and phase evolution during non-equilibrium solidification processes, which are relevant for ingot casting, DED-LB/M and PBF-LB/M. The Scheil simulations were conducted under different solidification velocities by employing the solute trapping model to explore the effect of thermal conditions on solidification and microsegregation behavior during non-equilibrium solidification processes. Here, the solute trapping model assumes that solute trapping occurs exclusively in the primary solid phase (primary phase being the sole dendrite forming phase). Hence, the quantity and composition of solid phases were influenced by the solute trapping induced by the change in solidification velocity. Consequently, the $Al_xCo_{25}Fe_{(50-x)}Ni_{25}$ compositional space is computationally screened between x = 10.5 and 16.5 (Fig. 1b) to investigate the evolution of B2-phase fraction and Al composition in liquid (i.e., Al is most intensively partitioned compound forming solute) under slow and rapid solidification velocities. Accordingly, the lower Al content (x = 10.5) was selected to induce a supersaturated single-phase fcc matrix upon solidification

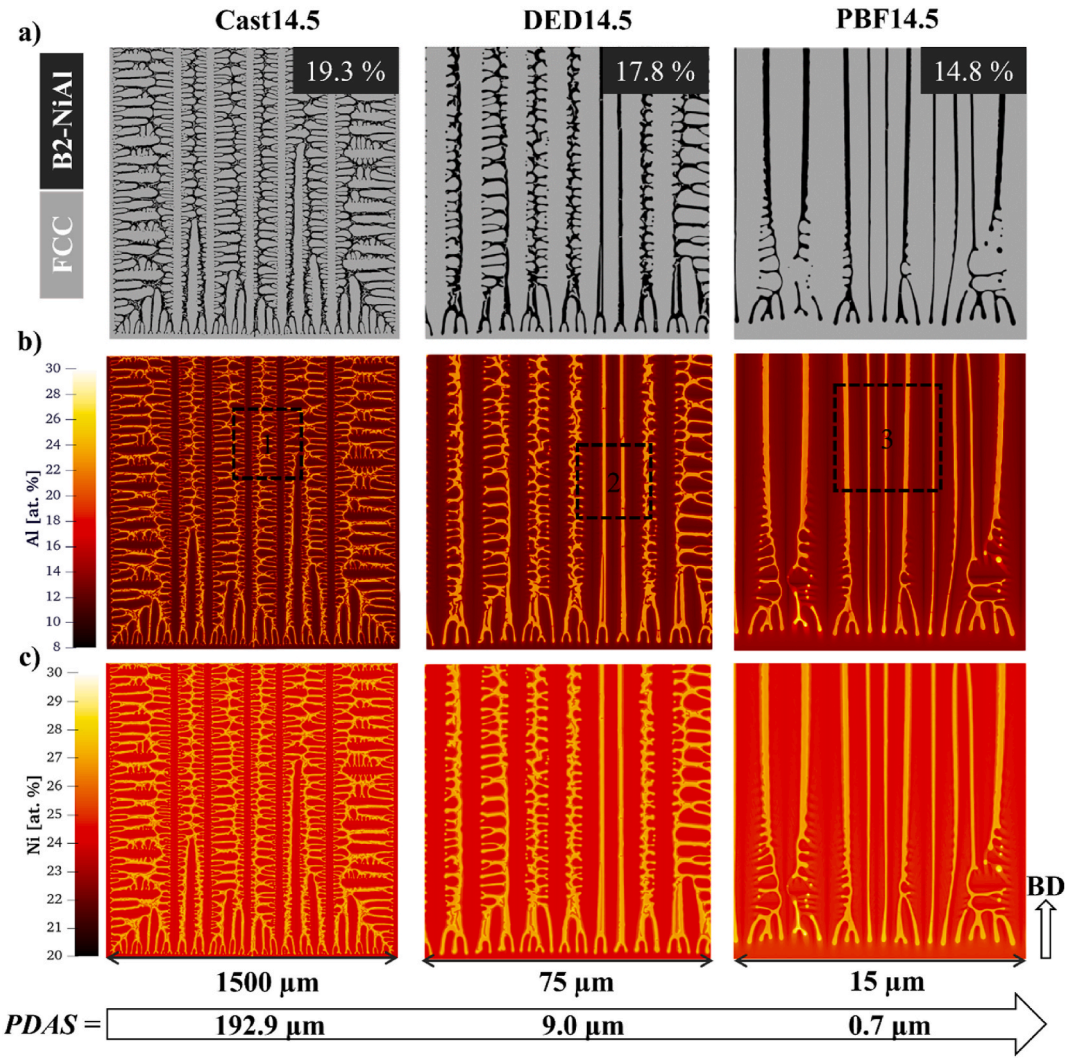

Fig. 3. Multiphase-field simulation results for the solidification of $Al_{14.5}Co_{25}Fe_{35.5}Ni_{25}$ alloy under thermal conditions resembling ingot casting, DED-LB/M and PBF-LB/M processes. BD shows the building direction for DED-LB/M and PBF-LB/M processes. (a) Phase maps, (b) Al and (c) Ni distributions maps. Black dashed boxes indicate the close-ups sectioned for the virtual EDX line scans in Fig. 4b. PDAS measurements for each process were taken along the complete cross-section. The values in the black boxes represent the B2-NiAl area fraction as determined from multiphase-field simulations.

(Fig. 1b), aiming to design a state directly eligible for aging heat-treatments to induce precipitation. In contrast, the larger Al content (x = 14.5) was opted to achieve dual-phase fcc-bcc microstructures in as-solidified state (Fig. 1b) to introduce a network-like B2-NiAl phase that aligns with the morphology and the size of the solidification structure. Here, the x = 10.5 at. % was the upper limit for obtaining a single-phase fcc in as-solidified state, based on Scheil solidification simulations. Any increase beyond this composition led to interdendritic B2-NiAl formation at the end of the solidification, as shown for the Scheil solidification simulations of x = 11 at. % in the supplementary section (Fig. S3). To visualize the effect of slow and rapid solidification, $Al_{10.5}Co_{25}Fe_{39.5}Ni_{25}$ alloy was selected, and results for solidification and microsegregation behavior are represented in Fig. 1c and d. For the $Al_{10.5}Co_{25}Fe_{39.5}Ni_{25}$ alloy, primary fcc solidification was predicted. The dendrite core (the first region to solidify) exhibited higher Fe and Co content, while the remaining melt in the interdendritic regions (the last region to solidify) was enriched with B2-NiAl stabilizing elements Ni and Al. Similar trends are also observed for $Al_{14.5}Co_{25}Fe_{35.5}Ni_{25}$ alloy. However, in the case of the $Al_{10.5}Co_{25}Fe_{39.5}Ni_{25}$ alloy, the Al quantity in the interdendritic regions were insufficient to stabilize B2-NiAl under both slow (R = 0.001 m/s) and rapid (R = 1 m/s) solidification velocities (Fig. 1b and d). Conversely, for the $Al_{14.5}Co_{25}Fe_{35.5}Ni_{25}$ alloy, there was enough accumulation of Al in the interdendritic regions (Fig. 1b) to stabilize the B2-NiAl phase, resulting in a predicted dual-phase solidification of fcc/B2-NiAl. The increase in solidification velocity for both compositions led to a decrease in the amount of Al in interdendritic regions due to enhanced solute trapping in primary fcc dendrites. This, in turn, resulted in a reduced quantity of B2-NiAl for the dual-phase $Al_{14.5}Co_{25}Fe_{35.5}Ni_{25}$ alloy (Fig. 1b).

It is essential to acknowledge that Scheil solidification simulations only provided a qualitative output to predict the segregation behavior and phase evolution under non-equilibrium solidification conditions, since these calculations do not completely cover the kinetics and do not resolve the microstructure during solidification. Consequently, while Scheil simulations provide valuable insights into the general trends of segregation and phase transformations, they should be complemented with more sophisticated modeling techniques or experimental observations for a comprehensive understanding of the solidification and microsegregation behavior. Therefore, a systematic quantitative investigation was undertaken through the complementary utilization of microstructure-resolved multiphase-field simulations followed by experimental characterization (Section 4.2.). These investigations aimed at exploring the influence of thermal conditions on key microstructural aspects, such as the evolution of dendritic microstructures and B2-NiAl

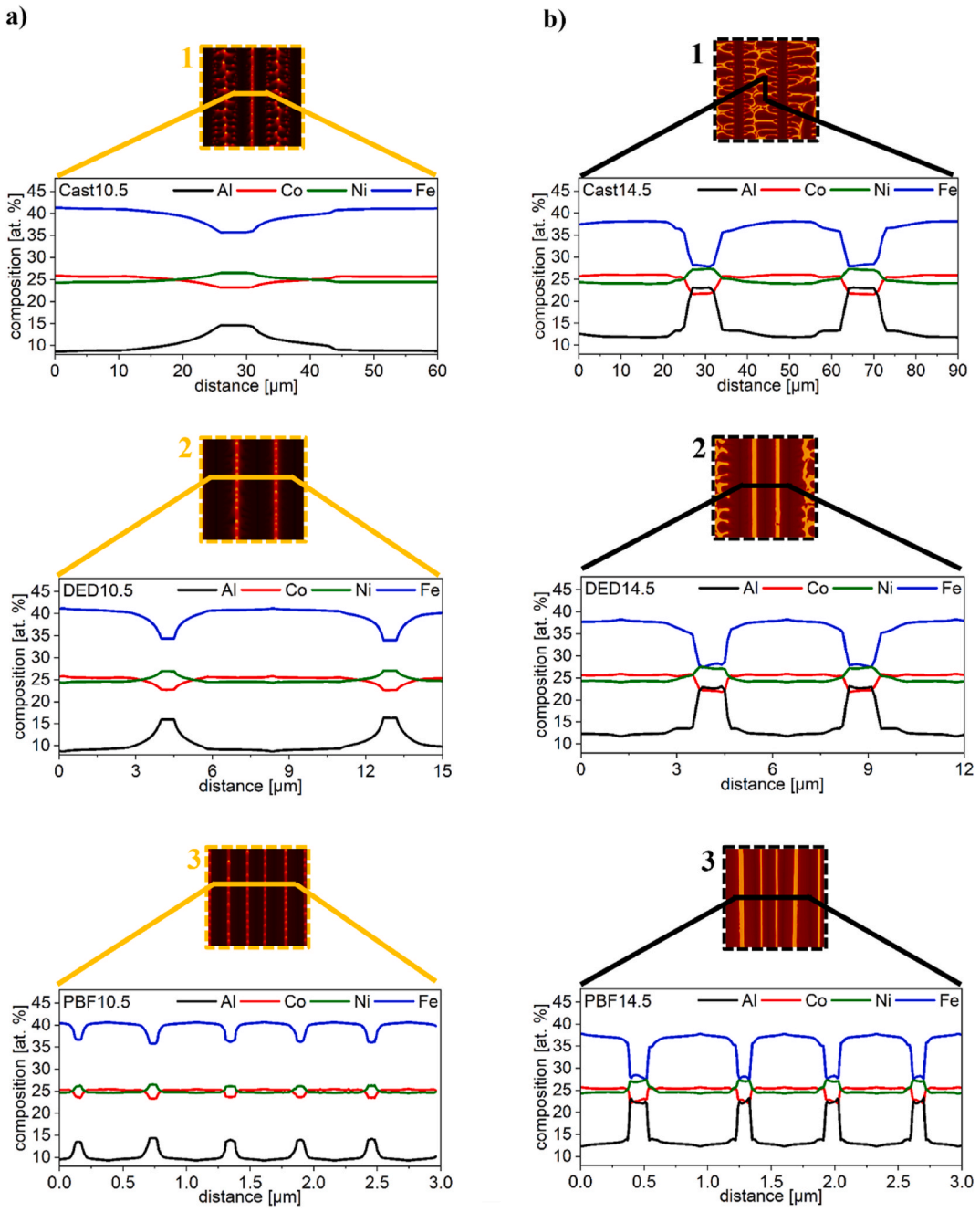

Fig. 4. Multiphase-field simulated microsegregation profiles of (a) $Al_{10.5}Co_{25}Fe_{39.5}Ni_{25}$ and (b) $Al_{14.5}Co_{25}Fe_{35.5}Ni_{25}$ alloys extracted by virtual EDX line-scans from the close-up sections shown in Figs. 2 and 3, respectively.

Table 3
Partition coefficients (k) calculated from the output of the multiphase-field simulations for the $Al_{10.5}Co_{25}Fe_{39.5}Ni_{25}$ and $Al_{14.5}Co_{25}Fe_{35.5}Ni_{25}$ alloys.

alloy	k_{Co}	k_{Fe}	k_{Ni}	k_{Al}
$Al_{10.5}Co_{25}Fe_{39.5}Ni_{25}$	1.07	1.18	0.94	0.72
$Al_{14.5}Co_{25}Fe_{35.5}Ni_{25}$	1.07	1.14	0.93	0.72

phase fractions, under specific solidification conditions resembling ingot casting, DED-LB/M, and PBF-LB/M. The multiphase-field simulation results for $Al_{10.5}Co_{25}Fe_{39.5}Ni_{25}$ and $Al_{14.5}Co_{25}Fe_{35.5}Ni_{25}$ alloys are depicted in Figs. 2 and 3, respectively, along with their corresponding virtual EDX line scans obtained from the simulations in Fig. 4. Additionally, the thermal conditions selected for the multiphase-field simulations are summarized in Table 1, and the partition coefficients (k) calculated from the output of the multiphase-field simulations for each alloy are presented in Table 3 to elaborate on the segregation behavior.

Upon reaching the liquidus temperature during cooling, the fcc phase was the primary solid phase for both compositions, independent from the experienced thermal conditions during solidification. As the fcc dendrites continued to grow into the liquid, segregation of Ni and Al into the liquid took place due to their lower solubility in the primary fcc phase and lower partition coefficients ($k_{Ni} = 0.94$ and $k_{Al} = 0.72$), while Fe and Co ($k_{Fe} = 1.18$ and $k_{Co} = 1.07$) were retained in the solid owing to their higher solubility, as can be seen in Fig. 4. In the case of the $Al_{14.5}Co_{25}Fe_{35.5}Ni_{25}$ alloy, the chemical gradients established between the fcc phase and liquid (Fig. 4) modified the local thermodynamic driving forces for phase transformations during dendritic solidification

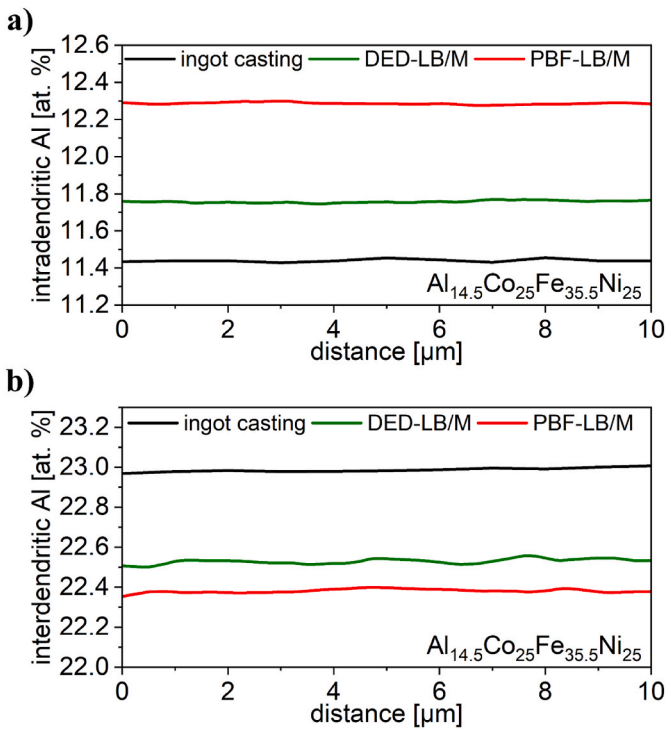

Fig. 5. Virtual EDX line-scans of (a) intradendritic and (b) interdendritic Al composition of the $Al_{14.5}Co_{25}Fe_{35.5}Ni_{25}$ alloy obtained from multiphase-field simulations under thermal conditions resembling ingot casting, DED-LB/M and PBF-LB/M processes. Distance denotes the length of the virtual EDX line-scans in the intradendritic and interdendritic regions.

(Fig. S4). This phenomenon eventually stabilized the B2-NiAl phase in the interdendritic regions at the end of the solidification (Fig. 3), whereas the Ni and Al accumulation was insufficient to stabilize interdendritic B2-NiAl in case of the $Al_{10.5}Co_{25}Fe_{39.5}Ni_{25}$ alloy (Fig. 2). Hence, the $Al_{10.5}Co_{25}Fe_{39.5}Ni_{25}$ alloy exhibited a single-phase fcc matrix with local compositional gradients, with the length scales being determined by the thermal conditions (Fig. 2).

The variations in thermal conditions had a significant impact on the dendrite spacing of the primary fcc phase as well as on the size and amount of the B2-NiAl phase. The primary dendrite arm spacing (PDAS) for the $Al_{10.5}Co_{25}Fe_{39.5}Ni_{25}$ alloy was calculated as 125.4 μm for ingot casting, 7.6 μm for DED-LB/M and 0.5 μm for PBF-LB/M simulations (Fig. 2). For the $Al_{14.5}Co_{25}Fe_{35.5}Ni_{25}$ alloy, the PDAS values were calculated as 192.9, 9.0 and 0.7 μm for ingot casting, DED-LB/M and PBF-LB/M, respectively (Fig. 3). Multiphase-field simulations evidenced that the dendrite spacing was reduced almost an order of magnitude as the cooling rate ($\dot{T}$) increases nearly three orders of magnitude during the transition between ingot casting, DED-LB/M and PBF-LB/M processes (Table 1). Likewise, the B2-NiAl fraction of $Al_{14.5}Co_{25}Fe_{35.5}Ni_{25}$ alloy also gradually decreased from 19.3 to 14.8 % between ingot casting and PBF-LB/M processes.

Change in thermal conditions also affected the solute partitioning during solidification. To showcase, virtual EDX line-scans of Al, e.g., the most intensively partitioned compound forming solute during solidification, were taken from intra- and interdendritic regions of $Al_{14.5}Co_{25}Fe_{35.5}Ni_{25}$ alloy, as shown in Fig. 5. The results indicated that the rapid solidification, established by the increase in $\dot{T}$ and solidification velocity (R), resulted in larger retainment of Al atoms in intradendritic fcc (dendrite core). Compared to ~11.4 at. % Al measured for ingot casting, the Al content increased to 11.7 at% Al for DED-LB/M process and to 12.3 at. % for PBF-LB/M process. In contrast, Al content in interdendritic regions was higher for ingot casting process compared to DED-LB/M and PBF-LB/M processes, with measured Al composition of 23.1, 22.6 and 22.4 at. % Al, for ingot casting, DED-LB/M and PBF-LB/M, respectively.

4.2. Experimental characterization

The microstructures of the $Al_{10.5}Co_{25}Fe_{39.5}Ni_{25}$ and $Al_{14.5}Co_{25}Fe_{35.5}Ni_{25}$ alloys, processed through ingot casting, DED-LB/M, and PBF-LB/M, were characterized using EBSD, as depicted in Figs. 6 and 7, as well as by optical microscopy (OM) and SEM-BSE (Fig. 8). The quantitative representation of the dependency of microstructural features on processing conditions was further elucidated in Fig. 9 and Table S1.

For $Al_{10.5}Co_{25}Fe_{39.5}Ni_{25}$ alloy, a single-phase fcc solidification was consistently observed from the phase maps independent of the processing conditions employed (Fig. 6a). The $Al_{14.5}Co_{25}Fe_{35.5}Ni_{25}$ alloy exhibited a dual-phase microstructure consisting of both fcc and bcc phases (Fig. 7). Notably, transitioning from ingot casting to PBF-LB/M process led to reduction in indexed bcc area fraction, decreasing from 23 % to 2 % (Fig. 7a). Furthermore, the effect of processing conditions on evolution of deformation related products, such as low-angle grain boundaries (LAGBs), high angle grain boundaries (HAGBs) and grain reference orientation deviation (GROD), was investigated in the fcc phase (primary solidified phase) (Fig. 6b-c and Fig. 7**b-c**). Here, the GROD misorientation maps demonstrated the angular deviation (in-grain misorientation) with respect to the mean orientation of a selected grain and characterize the degree to which a specific point within a grain is distorted or rotated relative to the mean orientation of the grain [46]. Therefore GROD can be essentially correlated with the deformation related local orientation gradients (orientation heterogeneities) [46]. For both compositions, the change in process-related thermal histories yielded increased LAGB fractions and mean GROD values. As a result, the PBF10.5 and PBF14.5 states exhibited the highest LAGB fractions and mean GROD values. Specifically, the PBF10.5 state showed LAGB fractions and mean GROD values of 39.8 % and 4.4°, while the PBF14.5 state exhibited corresponding values of 23.7 % and 3.4°, respectively (Table S1).

Fig. 8 shows dendritic microstructures and measured dendrite size spacings of $Al_{10.5}Co_{25}Fe_{39.5}Ni_{25}$ and $Al_{14.5}Co_{25}Fe_{35.5}Ni_{25}$ alloys processed by ingot casting, DED-LB/M and PBF-LB/M. The imaging methods and corresponding surface treatments of the samples were carried out based on the feature size of the as-solidified microstructures. The main comparison with respect to the length scale and morphology of the solidification structures was performed based on PDAS values for simplification. The PDAS values for Cast10.5 and Cast14.5 states were measured as 164.8 ± 27.6 and 142.8 ± 31.7 μm, respectively. The increase in cooling rate led to an order of magnitude decrease in PDAS values for DED10.5 and DED14.5 states compared to ingot cast states. This resulted in PDAS values of 12.7 ± 2.2 and 10.8 ± 2.2 μm, respectively. Further increase of cooling rates during PBF-LB/M process yielded the smallest PDAS values and morphologies for both alloys, measured as 0.8 ± 0.2 μm for the PBF10.5 state and 0.7 ± 0.2 μm for the PBF14.5 state. The experimental PDAS values and corresponding morphological trends closely resembled those obtained from multiphase-field simulations (Figs. 2 and 3). Specifically, the increase in solidification velocities and cooling rates resulted in the refinement of the final microstructure, e.g., after PBF-LB/M process, consistent with the predictions of the phase-field simulations. Moreover, increased cooling rates and solidification velocities due to AM-inherent confined melt-pools yielded a combination of several notable effects, as depicted in Fig. 9, with the corresponding data being provided in Table S1. They did not only refine the dendrite spacings and size of the B2-NiAl phase to submicron scales and reduce the fractions of B2-NiAl phase, but these conditions also effectively facilitated characteristic structural modifications of the final microstructure. This was evidenced by an increase in the fraction of LAGBs and mean GROD values. Hence, refinement of dendrites and corresponding microsegregation patterns were accompanied by an increase in structural heterogeneity of the microstructure, particularly pronounced in the case of the PBF-LB/M process.

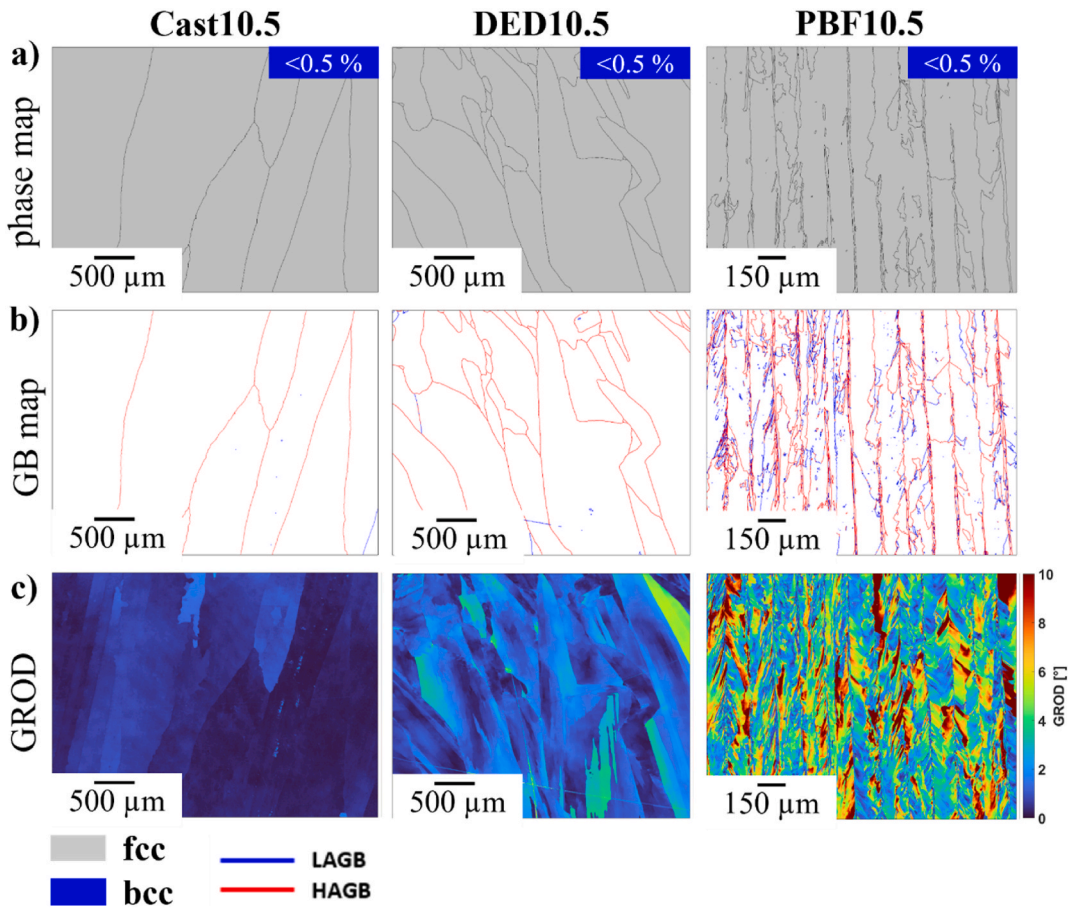

Fig. 6. EBSD analysis of Cast10.5, DED10.5 and PBF10.5 states. a) phase maps, b) grain boundary (GB) maps and c) grain reference orientation deviation (GROD) maps. High-angle grain boundaries (HAGB) were defined by a misorientation angle $\Theta > 10°$, whereas low-angle grain boundaries (LAGB) were defined by $2 \leq \Theta \leq 10°$. The values in the blue boxes represent the measured bcc area fractions.

To understand the compositional characteristics and to unveil microsegregation profiles of intra- and interdendritic regions (Fig. 8), EDS elemental maps and quantitative line-scans were conducted, as demonstrated in Figs. 10 and 11. For all states, a consistent trend emerged: the Al and Ni, e.g., elements with $k < 1$ (Table 3), enriched in interdendritic regions, whereas intradendritic regions were enriched in Co and Fe. However, analogous to the predictions from Scheil solidification and phase-field simulations (Figs. 1, 2 and 3), irrespective of the processing method employed, the chemical gradients established between liquid and fcc phase were insufficient to induce the formation of interdendritic B2-NiAl phase in the $Al_{10.5}Co_{25}Fe_{39.5}Ni_{25}$ alloy (Fig. 10a–c and 11a). On the other hand, the Al and Ni enrichment in liquid during the solidification of $Al_{14.5}Co_{25}Fe_{35.5}Ni_{25}$ alloy substantially modified the local thermodynamic driving forces for phase transformations during dendritic solidification (Fig. S4). This modification led to the formation of interdendritic B2-NiAl phase (Fig. 10b–d and 11b), with its morphology, size and fraction being determined by thermal conditions.

5. Discussion

5.1. Simulation-based assessment and experimental validation of as-solidified microstructures and their evolution

The simulations and experimental results were in a good agreement regarding microsegregation behavior, effect of thermal conditions on microstructural length scales and the combined influences of both phenomena on phase evolution.

Based on the predictions from simulations, Al exhibited a strong inclination for positive segregation, whereas Ni also enriched in the same direction, albeit to a lesser extent. Fe and Co segregation were predicted to take place in the opposite direction, indicating an enrichment in the primary solid. The experimental results (Figs. 10 and 11) validated the computational predictions (Figs. 1 and 4) in terms of microsegregation behavior. The elements with $k < 1$, e.g., Al and Ni, expectedly accumulated in the liquid, showing microsegregation in interdendritic regions, whereas Fe and Co were mainly distributed in dendrite cores ($k > 1$, Table 3). As suggested by simulations, Al supersaturation occurred without forming interdendritic B2-NiAl phase in the $Al_{10.5}Co_{25}Fe_{39.5}Ni_{25}$ alloy and dual-phase microstructures formed in the $Al_{14.5}Co_{25}Fe_{35.5}Ni_{25}$ alloy, which satisfied the design criteria of both alloys.

Moreover, the combination of multiphase-field simulations (Figs. 2 and 3) and experimental characterization (Fig. 8) showed that rapid solidification associated with AM-processes led to finer dendritic structures with sub-micron scale PDAS in the case of PBF-LB/M samples. At lower cooling rates, e.g., during ingot casting, low degrees of undercooling (ΔT) were generated, ($\Delta T_{min} = 0.2$ K according to multiphase-field simulations), which reduced the number of nucleation events and promoted coarsening of the dendrites. This ultimately resulted in larger dendrite arm spacings and a higher volume fraction of interdendritic regions (length scale of Al and Ni microsegregation) at the end of solidification [2,47]. In contrast, the increase in cooling rate, e.g., as in the PBF-LB/M process (Figs. 2 and 3), the ΔT subjected to the liquid at a given time was enhanced ($\Delta T_{min} = 19.6$ K according to multiphase-field simulations). Consequently, the increase in ΔT increased driving force

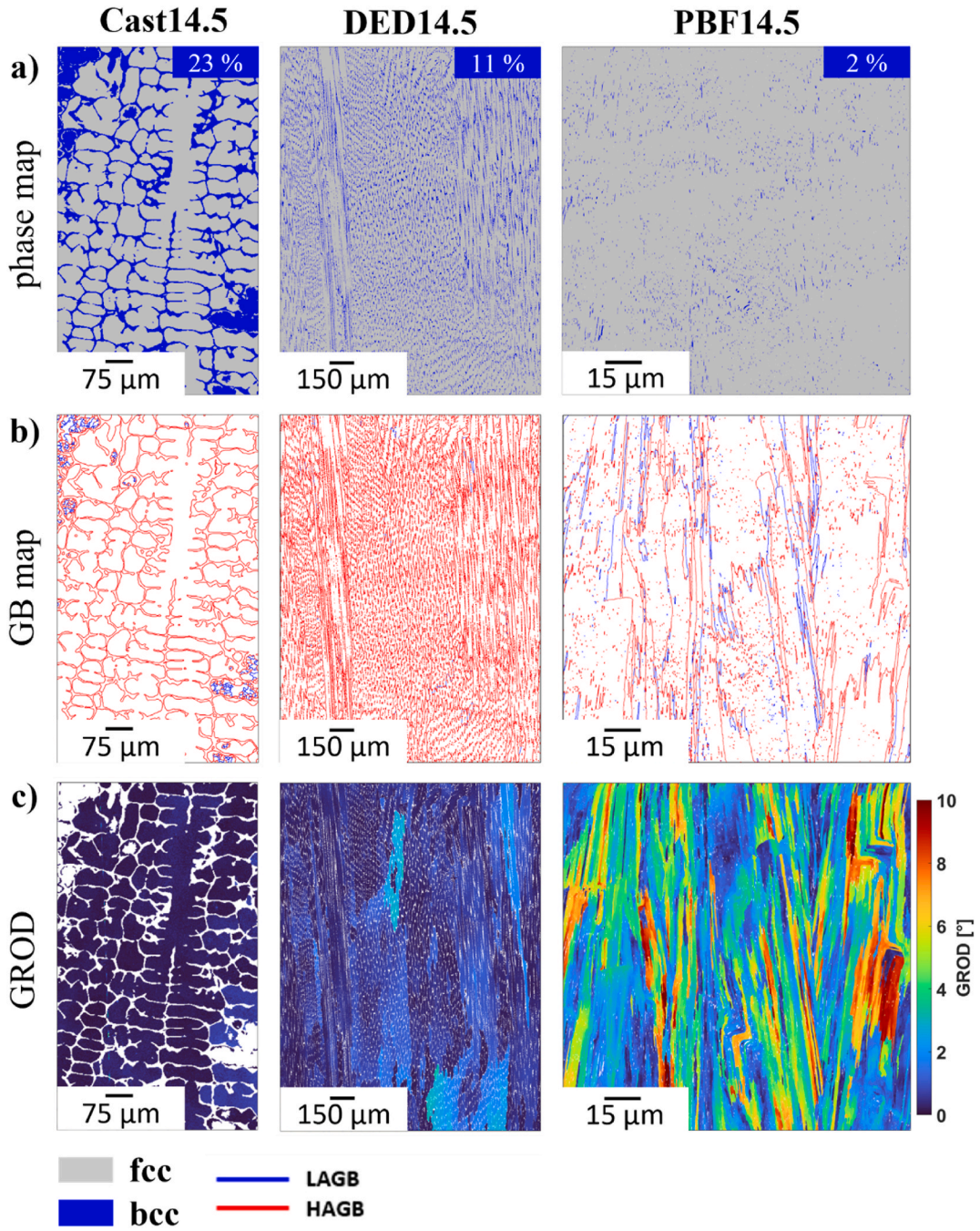

Fig. 7. EBSD analysis of Cast14.5, DED14.5 and PBF14.5 states. a) phase maps, b) grain boundary (GB) maps and c) grain reference orientation deviation (GROD) maps. High-angle grain boundaries (HAGB) were defined by a misorientation angle $\Theta > 10^{\circ}$, whereas low-angle grain boundaries (LAGB) were defined by $2 \leq \Theta \leq 10^{\circ}$.The values in the blue boxes represent the measured bcc area fractions.

for solidification, promoted formation of more solid-liquid interface per unit volume and faster dendrite growth rates [2,47]. This, in turn, resulted in refinement of the length scale and spacing of the intra- and interdendritic regions as evidenced by transition from ingot casting to DED-LB/M and PBF-LB/M processes in Figs. 2, 3 and 8 [14]. Finally, when the liquid is confined in such fine interdendritic regions, it gave rise to ultra-fine scale microsegregation patterns in single-phase fcc matrix or ultra-fine B2-NiAl phase at the end of the solidification. The width of these interdendritic regions was as thin as 76.4 ± 15.9 nm and 46.9 ± 8.8 nm for PBF10.5 and PBF14.5 states, respectively, according to experimental characterization from SEM and STEM micrographs (Fig. 11), respectively.

Transitioning from thermal conditions associated with ingot casting to DED-LB/M and PBF-LB/M processes resulted in decreased fractions of the B2-NiAl phase, as can be seen from multiphase-field simulations (Figs. 2 and 3) and experimental characterization (Figs. 6 and 7). The decrease in B2-NiAl content was attributed to the decrease in solute partitioning over the fast moving solid-liquid interface (high R), resulting in insufficient time for solute elements to diffuse and redistribute into the liquid. As a consequence, the excess solute was retained in the primary solid phase during solidification [48–51] and the primary solid phase accumulated higher solute content during DED-LB/M ($R = 1$ cm/s) and PBF-LB/M ($R = 10$ cm/s), as compared to ingot casting ($R = 0.1$ cm/s). This led to a gradual reduction in Ni and Al contents in the liquid phase (Fig. 5), which simultaneously reduced the non-equilibrium solidification range and corresponding B2-NiAl content at the end of

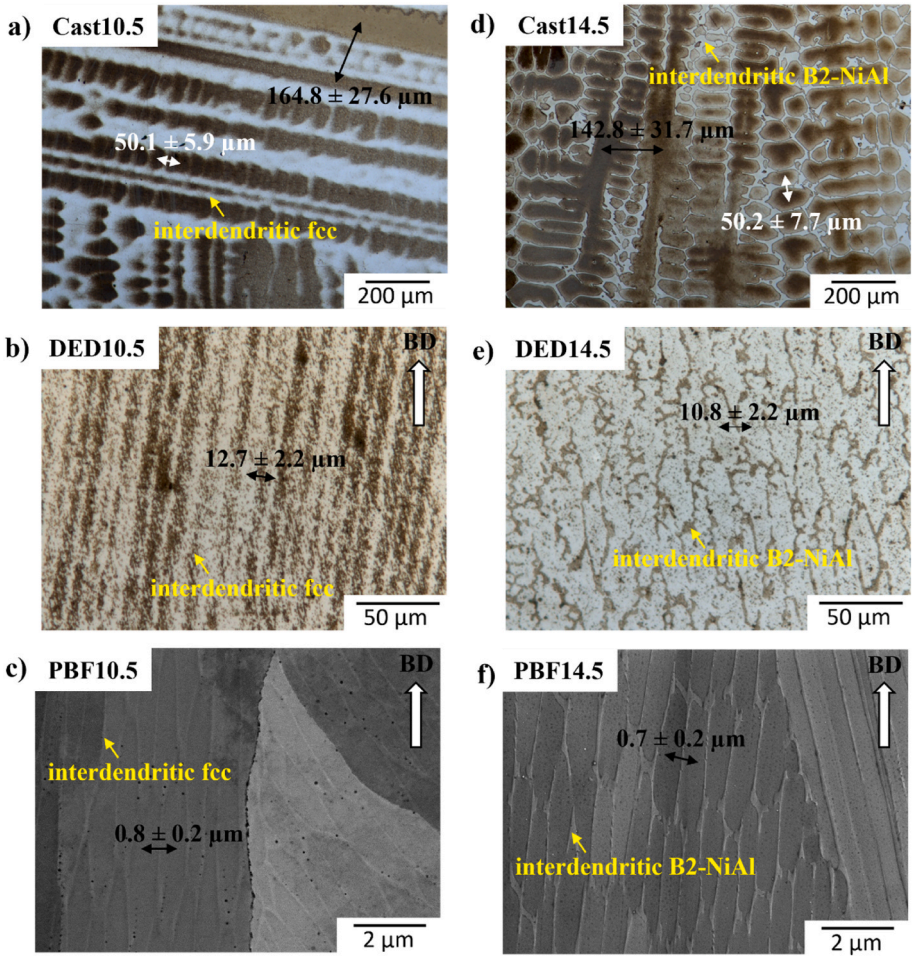

Fig. 8. Dendrite arm spacing measurements performed by LOM on color etched samples and SEM-BSE on electropolished samples. The spacings were determined by measuring the distance between the cores of adjacent dendrites in multiple micrographs, and average values are presented. Black arrows indicate PDAS values, whereas white ones show SDAS values. Yellow arrows show interdendritic regions and corresponding phases. The imaging methods were selected based on feature size of as-solidified microstructures. a) LOM of Cast10.5 state, b) LOM of DED10.5 state, c) SEM-BSE of PBF10.5 state, d) LOM of Cast14.5 state, e) LOM of DED14.5 state and f) SEM-BSE of PBF14.5 state.

solidification (Figs. 1, 3 and 7). Therefore, the decrease in B2-NiAl content in the DED14.5 and PBF14.5 states can be attributed to a combination of factors: i) the reduction of the composition of B2-NiAl stabilizing elements Ni and Al in the liquid phase (interdendritic regions) due to solute trapping at high solidification velocities (Figs. 1 and 5), and ii) the decrease in liquid area fraction resulting from the refinement of the dendritic structure due to the increase in ΔT associated with high cooling rates during rapid solidification. The results clearly demonstrated the flexibility in tuning the size, amount, and morphology of B2-NiAl through the adjustment of solidification conditions.

Lastly, transitioning from ingot casting to additive manufacturing notably altered further structural characteristics of the final microstructure, such as the fraction of HAGBs, LAGBs and mean GROD values, as described in Fig. 9 and Table S1. These alterations were rather prominent in the states produced by PBF-LB/M, whereas the DED-LB/M states underwent relatively minor modifications in comparison to the ingot-cast states. High fractions of LAGBs are generic for metals processed via PBF-LB/M [52–54] and higher dislocation densities are observed in the vicinity of LAGBs [55,56]. Accordingly, the presence of larger fractions of LAGBs and mean GROD values can be interpreted as a degree of heterogeneity caused by deformation that evolves from complex thermal histories due to iterative melting-solidification [57] and heating-cooling cycles in combination with high cooling rates, temperature gradients and solidification velocities [38,58] during AM processes. As a result, the AM-inherent thermal conditions not only refined the dendrite spacings and the size of the B2-phase, but also effectively modified the structural characteristics of the final microstructures by accommodating larger elastic and plastic strains throughout the process [20].

5.2. *Segregation-guided alloy design approach using tailored solidification behavior*

The ability to tune the size, morphology and crystal structure of microstructural features is of utmost importance in engineering applications, e.g., for the design of structural components. Thermal conditions, such as the cooling rate, play a significant role in adjusting such specifics of the microstructure during solidification, allowing for the formation of both finer and coarser domains in microstructures based on the intended application case and environment. Fundamentally, various thermal conditions can be achieved in any solidification process, however, unique processing conditions inherent to AM facilitate an unmatched advantage in terms of site-specific microstructure design [19], while circumventing undesired macrosegregation associated with traditional casting methods. Accordingly, the core concept of “segregation-guided alloy design” approach relies on modifying the alloy matrix through a range of solidification conditions with cooling rates varying over six orders of magnitude. In this context, the aim was to achieve matrix design by manipulating the solidification behavior and microsegregation phenomenon by means of alloy composition and

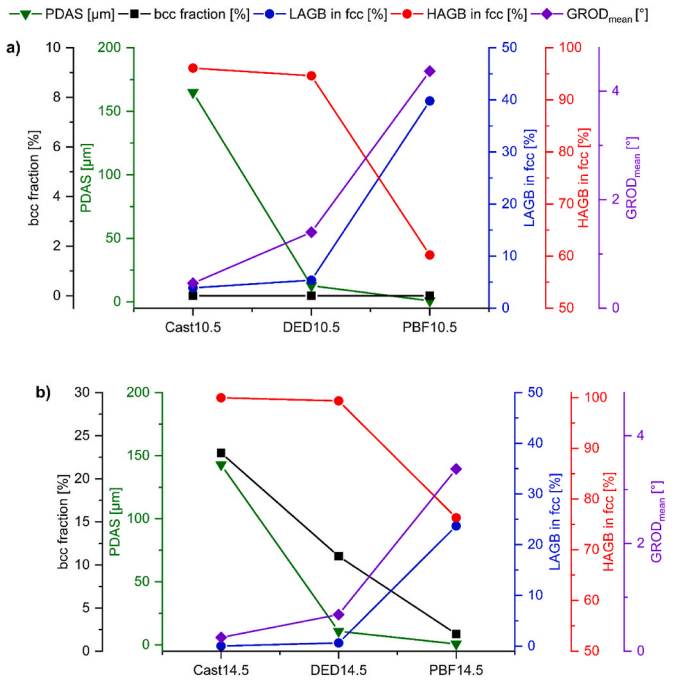

Fig. 9. Change in microstructural features with respect to fabrication process and related thermal conditions. a) $Al_{10.5}Co_{25}Fe_{39.5}Ni_{25}$ alloy and b) $Al_{14.5}Co_{25}Fe_{35.5}Ni_{25}$ alloy.

control of thermal conditions during solidification processes. The current study exemplified this concept and demonstrated how the length scales, site-specific compositions and crystal structures of dendritic microstructures were altered by leveraging thermodynamics and solidification kinetics. This was achieved by utilizing a novel $Al_xCo_{25}Fe_{(50-x)}Ni_{25}$ alloy (with x = 10.5 and 14.5 at. %) as a model system capable of forming both single- and dual-phase microstructures during solidification. However, specific prerequisites are necessary to effectively apply this design perspective to a broad range of alloys.

To design new microstructures by tailored solidification, a comprehensive understanding of the relationship between alloy composition and processing conditions is necessary. Essentially, the interplay of alloy composition (partition coefficients of alloying elements) and thermal conditions (degree of undercooling and solid-liquid interface velocities) during solidification determines both the spatial frequency of solidification cell boundaries (e.g., PDAS) and the amplitudes of intra- and interdendritic elemental compositions, as shown by simulations (Figs. 2 and 3) and experimental characterization (Figs. 8, 10 and 11). Modern efforts, such as Integrated Computational Materials Engineering (ICME), provide a powerful methodology that assists in not only the rapid evaluation of potential compositions through thermodynamic modeling and Scheil solidification simulations but also the prediction of corresponding microstructure evolution during non-equilibrium solidification via multiphase-field modeling. Using such tools, compositional gradients between intradendritic (e.g., primary solid) and interdendritic (e.g., liquid) regions can be calculated. Therefore, modeling of the effects of elemental partitioning on phase stabilities, driving forces for phase transformations, and solidification intervals of the alloys helps to program solidification and nucleation conditions. Consequently, selective enrichment of desired elements between solid and liquid can promote various phenomena, such as the enrichment of compound-forming elements in interdendritic regions (Figs. 2, 10 and 11a), stabilization and distribution of secondary phases in interdendritic regions (Figs. 3, 10 and 11b), or as reported in other studies, mitigation of cracking during rapid solidification [6–10].

Fig. 12 summarizes the concept of segregation-guided alloy design through tailored solidification behavior. The selection of the nominal composition (X_N) is guided by thermodynamics to design alloys suitable for targeted criteria, such as age hardening. Shifting of the nominal composition towards left or right corners of the representative phase diagram changes the content of alloying elements, which are responsible for tailoring microstructure evolution during and after solidification. For simplicity, two sets of elements are defined: element class A and element class B. Element class A consists more of primary phase stabilizers (in this case, phase 1), whereas element class B includes targeted elements for microsegreation to tailor solidification behavior, such as stabilizing phase 2 to obtain dual-phase microstructure. Increasing the composition towards element class B-rich side of the phase diagram enhances their partitioning in the liquid until phase 2 becomes the primary phase to solidify. The change in X_N allows adjustable retention of element class B in interdendritic regions after non-equilibrium solidification. Moreover, during non-equilibrium solidification, the length scales of the dendrites are mediated by the ΔT imposed by the thermal conditions during solidification (Figs. 2, 3, 10, and 11). Thus, the X_N enables modification of the amount of B class elements within interdendritic regions, subsequently governing local composition and properties of the alloy, whereas the length scales of local gradients are determined by ΔT during solidification. Consequently, this results in local property gradients, such as chemical driving force for phase transformation, driven by the variations in local composition within the dendritic structure of the tailored alloy matrix, inherited from non-equilibrium solidification.

For instance, in current study, compound forming elements, such as Al and Ni as B2-former, were incorporated into interdendritic regions of the single-phase fcc matrix (Fig. 11a) to predetermine the microstructures prior to aging treatment, thereby, to locally control the precipitation kinetics and phase-transformation pathways, as can be seen in Fig. 13. Here, the incorporation of Al and Ni into the nanoscale interdendritic regions after PBF-LB/M of $Al_{10.5}Co_{25}Fe_{39.5}Ni_{25}$ alloy amplified the local driving force for B2-precipitation during aging treatments (Fig. 13a), leading to the formation of the B2-phase (ordered bcc, $B2_{(100)}$ superlattice reflection is visible) solely within the nanoscale interdendritic regions as evidenced morphologically and structurally in Fig. 13b and c. Thus, the metal matrix formed by rapid solidification acted as a template, where the B2-phase can be deliberately positioned into predetermined locations with higher chemical driving forces for phase transformation. Hence, this approach can provide design and exploration of composite-like microstructures through AM and post-AM heat-treatments, where the morphology of the dendritic structures, thereby the distribution of the secondary phases, can also be altered by AM-processing parameters. Furthermore, by increasing the Al composition, as in $Al_{14.5}Co_{25}Fe_{35.5}Ni_{25}$ alloy, interdendritic regions can be decorated with secondary phases as showcased in multiphase-field simulations (Fig. 3) and experiments (Figs. 10 and 11). In this case, the morphology of the solidification structure effectively determined the size and distribution of the B2-phase, which was adjusted by the degree of undercooling during employed ingot casting and AM processes. Specifically, the PBF-LB/M process rendered highest cooling rates and solidification velocities, yielding a homogenous distribution of ultra-fine B2-NiAl phase (thickness ~ 47 nm) across the fcc matrix. Hence, this approach is projected to fine-tune the size and morphology of dual-phase microstructures through segregation-mediated phase nucleation and growth during solidification. This capability can eliminate the need for post-processing to control the size and distribution of the second phases in the alloy matrix.

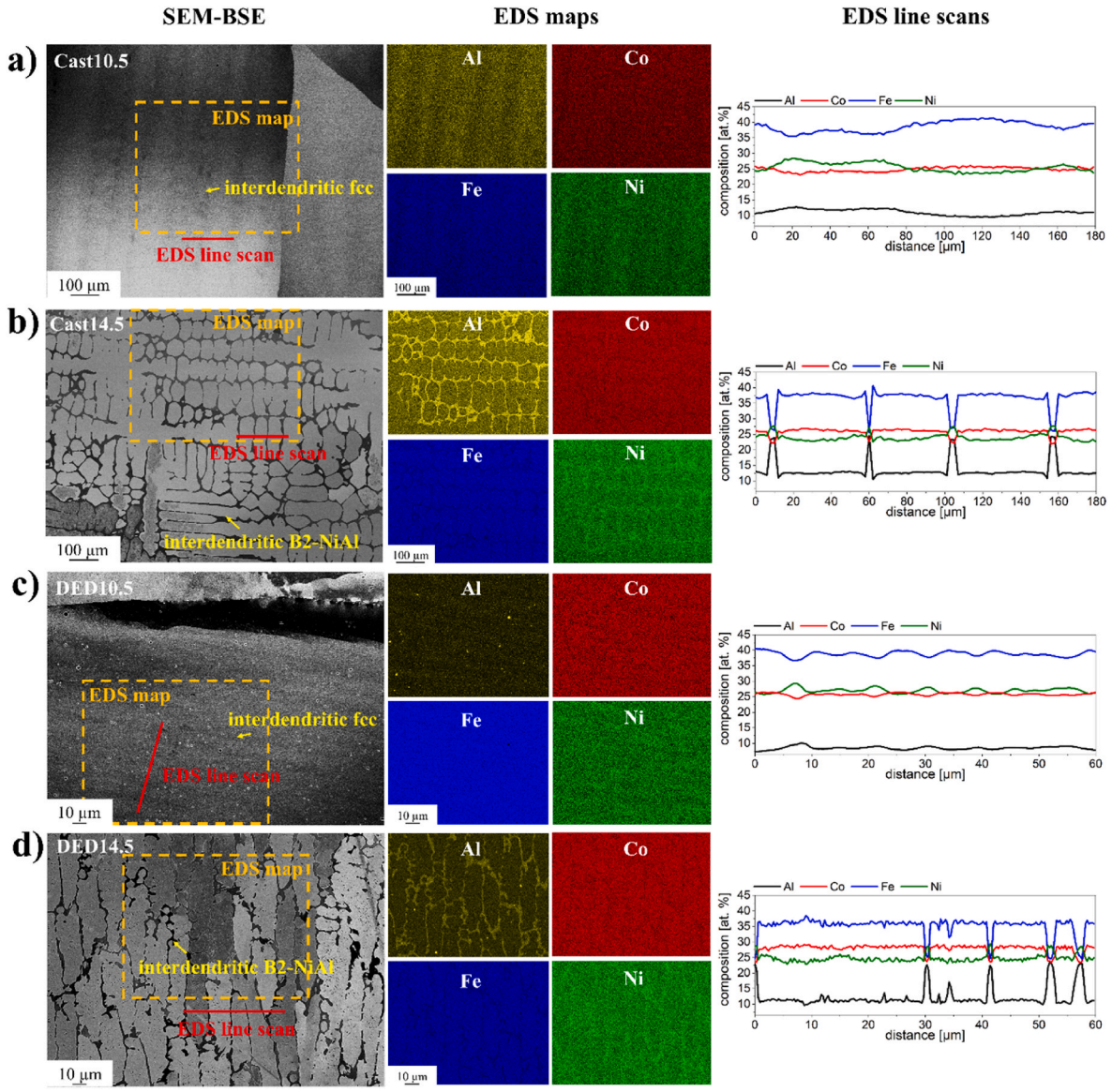

Fig. 10. EDS elemental maps and line-scans performed on ingot cast and DED-LB/M states of $Al_{10.5}Co_{25}Fe_{39.5}Ni_{25}$ and $Al_{14.5}Co_{25}Fe_{35.5}Ni_{25}$ alloys. Dashed rectangles and red lines in the SEM-BSE images show the regions selected for EDS maps and line-scans, respectively. a) Cast10.5 state, b) Cast14.5 state, c) DED10.5 state and d) DED14.5 state.

In addition to the specific examples provided with the designed $Al_xCo_{25}Fe_{(50-x)}Ni_{25}$ MPEA system, the presented approach holds promise for wide variety of cases across different alloys, for instance, designing microstructures with locally varying stacking fault energies (SFEs) [12]. By deliberately adjusting compositional fluctuations, such as Mn, Al and C content, between dendrite cores and interdendritic regions through thermal conditions and alloy composition, local gradients in SFEs and austenite stability can be achieved [13]. These gradients significantly influence local phase stabilities and the tendency to form martensite in regions of low austenite stability. Such adjustments potentially enable the modification of local deformation behavior, such as transformation-induced plasticity (TRIP), twinning-induced plasticity (TWIP), or dislocation slip, depending on the region within the microstructure, which can initiate their simultaneous or sequential activation, whereas the size of these regions can be flexibly tuned by employed thermal conditions during solidification. Moreover, the proposed approach can be applied to design heterogeneous/heterostructured materials with tunable mechanical properties by intentionally incorporating both soft and hard domains [59,60]. In such materials, the deformation behavior can be adjusted through back-stress strengthening and work hardening [59], which is significantly influenced by the size, morphology, distribution, and volume fraction of constituent phases. Such flexibility in design is exemplified by the $Al_{14.5}Co_{25}Fe_{35.5}Ni_{25}$ MPEA with soft fcc and hard B2-NiAl domains in this study, where the size, distribution, and morphology of the hard B2-NiAl phase were aligned with the solidification morphology of the solidification microstructure, while its volume fraction was controlled via the thermal conditions. Finally, the economic importance of designing and developing materials capable of withstanding harsh environments for extended service times is crucial, particularly concerning aspects like

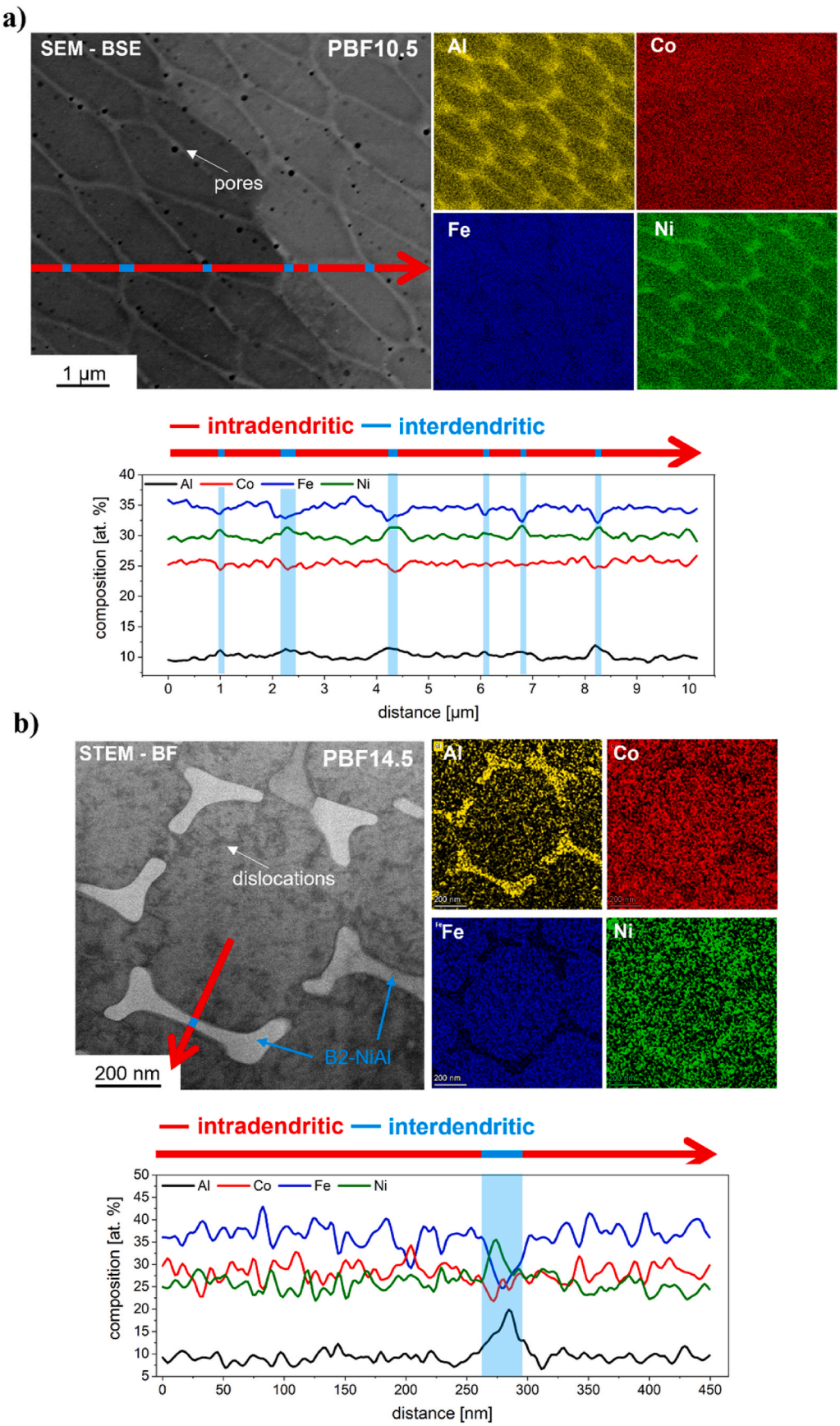

Fig. 11. EDS elemental maps and line-scans conducted on PBF-LB/M states of $Al_{10.5}Co_{25}Fe_{39.5}Ni_{25}$ and $Al_{14.5}Co_{25}Fe_{35.5}Ni_{25}$ alloys via SEM-EDS and STEM-EDS, respectively. Red arrows in micrographs demonstrate EDS line-scans, while the interdendritic regions were indicated with light blue color. a) PBF10.5 and b) PBF14.5 states.

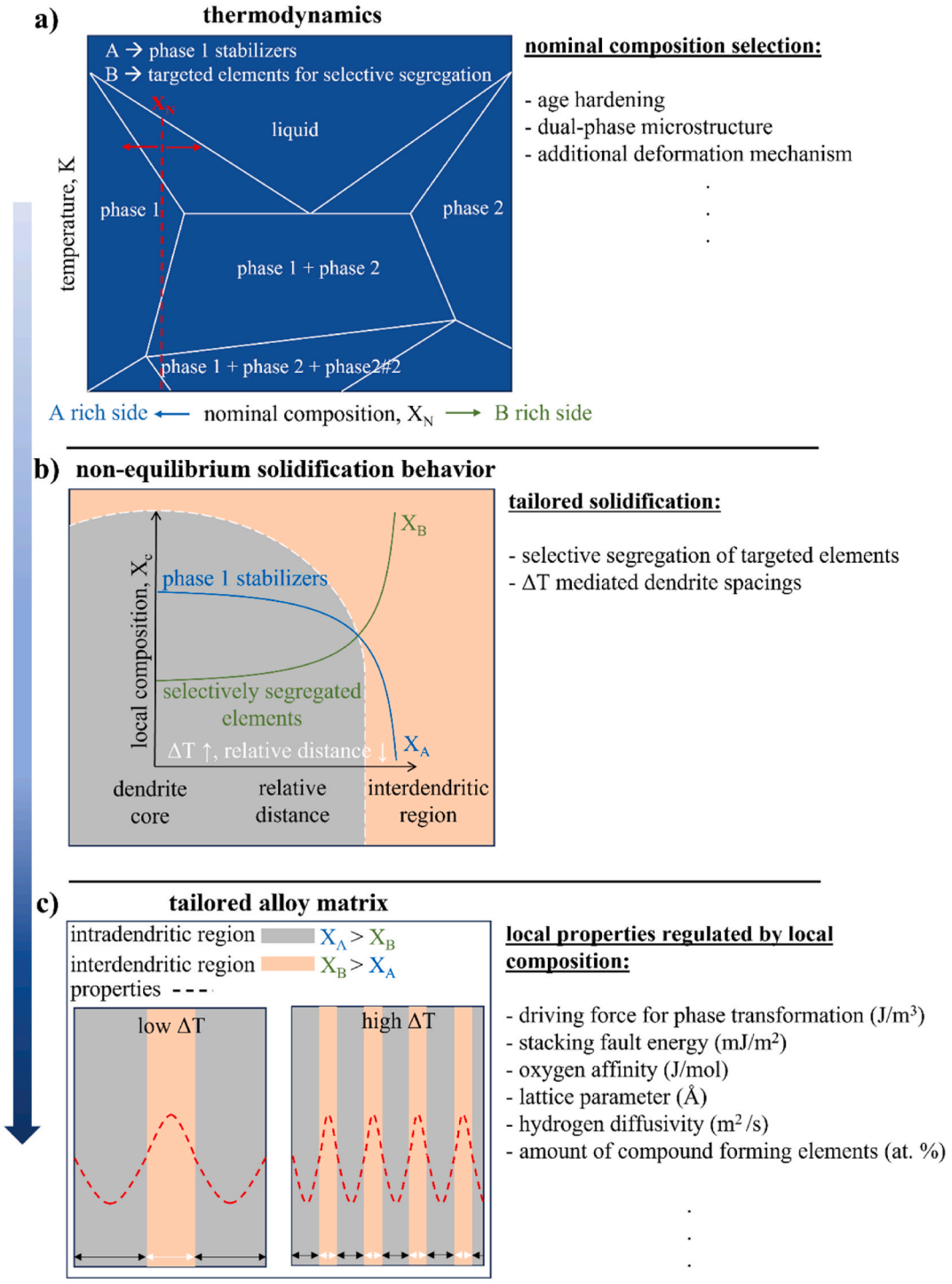

Fig. 12. Concept of segregation-guided alloy design by tailored solidification behavior. a) Thermodynamics guided nominal composition selection based on alloy design criteria. b) Partitioning of targeted elements in liquid during non-equilibrium solidification. This step leads to local composition gradients after non-equilibrium solidification, while their length scales were determined by ΔT during solidification. c) Tailored alloy matrix with local property gradients between intra- and interdendritic regions adjusted via local composition gradients inherited from non-equilibrium solidification.

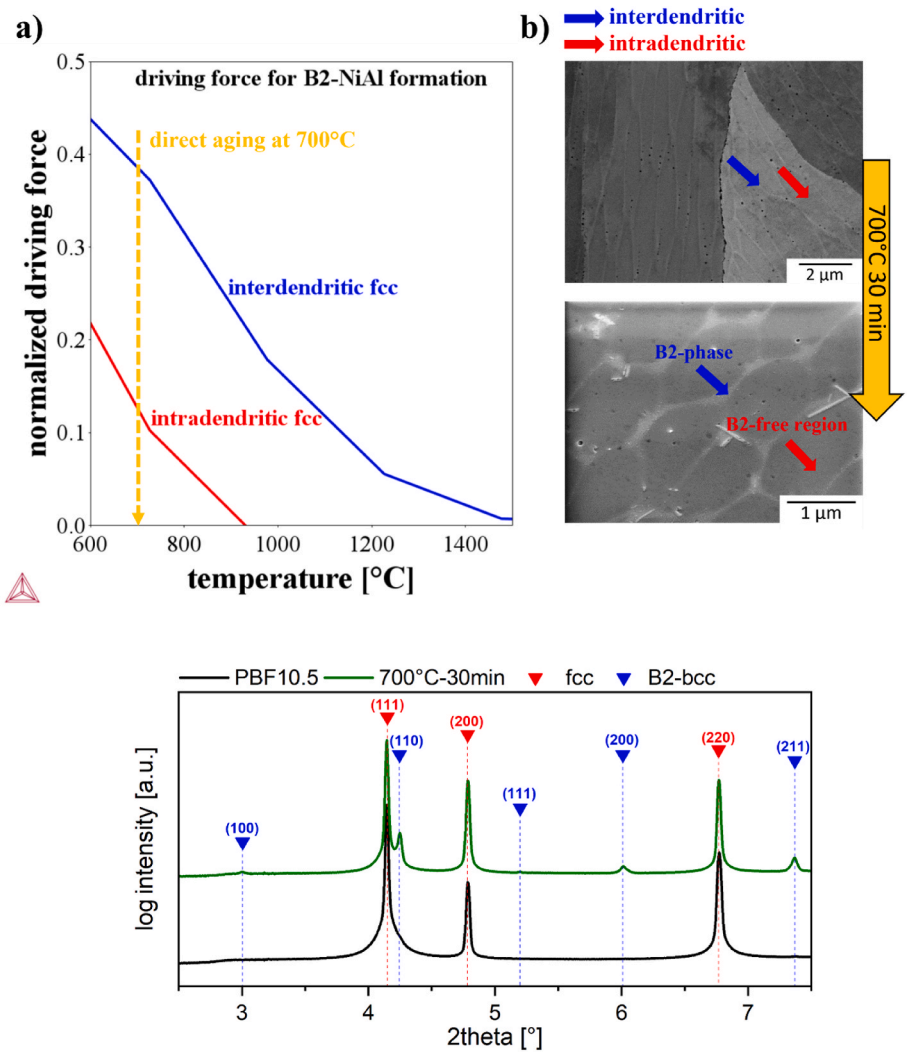

Fig. 13. a) Normalized driving force for B2-NiAl formation for PBF10.5 state as a function of temperature. Calculations were performed using the software Thermo-Calc® upon implementing the intra- and interdendritic fcc compositions of PBF10.5 state acquired from multiphase-field simulations. b) The microstructure evolution after aging at 700 °C for 30 min revealed the initiation of nanoscale B2-precipitates at interdendritic regions, where Ni and Al enrichment provided a high chemical driving force for B2-formation. c) SYXRD measurements of PBF10.5 in as-built and aged (700 °C-30 min) condition.

corrosion and hydrogen embrittlement behavior. The size and properties of the intra- and interdendritic regions can be engineered through tailored solidification behavior, while structural gradients, such as the fraction of LAGBS and dislocation densities amongst dendritic structures [17,61–63] can be flexibly controlled using AM techniques. These methods may further be utilized to achieve reduced damage, increased corrosion and hydrogen embrittlement resistance [17], though further investigations are required to explore these capabilities, especially in context of AM materials [61,64].

Lastly, the scope of this study was focused on validating the interdependencies between segregation behavior and the resulting microstructure characteristics generated under different solidification conditions, with the aim of fundamentally assessing the feasibility of the proposed segregation-guided design concept. While it is acknowledged that major microstructural changes were not demonstrated within the same process -such as generating gradients in alloy chemistry or processing conditions in situ across different sample heights- the potential to modify microstructures across a broad range of conditions was successfully presented. These possibilities can be further expanded by AM techniques like high-speed directed energy deposition (HS-DED), which can emulate a wide range of thermal conditions, e.g. covering those of DED-LB/M and PBF-LB/M [65], and enable in situ modification of chemical compositions and process conditions, allowing for versatile control of dendritic microstructures.

6. Summary and conclusions

In this study, a perspective on segregation-guided alloy design via tailored solidification was presented. Our approach focused on tailoring the length scales of the dendritic microstructures and corresponding site-specific, e.g., interdendritic, compositional and structural characteristics of the alloy matrix formed as a product of solidification. This was achieved by controlling the microsegregation behavior through nominal alloy composition and thermal conditions of the solidification processes, e.g., with modified cooling rates ranging over six orders of magnitude. To this end, two model alloys, namely $Al_xCo_{25}Fe_{(50-x)}Ni_{25}$

multi-principal element alloys (MPEA) with x = 10.5 and 14.5 at. %, yielding in single-phase and dual-phase microstructures were successfully designed from the Al-Co-Fe-Ni compositional space through computational alloy selection by using CALPHAD and Scheil solidification simulations. Multiphase-field simulations were utilized to elucidate the combined influence of alloy composition and thermal conditions on the microstructure evolution under a range of solidification conditions corresponding to ingot casting, directed energy deposition (DED-LB/M) additive manufacturing (AM), and laser powder bed fusion (PBF-LB/M) AM. Lastly, the use of selective enrichment of desired elements in interdendritic regions was experimentally displayed for PBF-LB/M fabricated $Al_{10.5}Co_{25}Fe_{39.5}Ni_{25}$ alloy and its potential extension to other applications was critically discussed. The following conclusions can be drawn:

- The increase in nominal Al composition altered the microsegregation behavior during solidification. In the $Al_{10.5}Co_{25}Fe_{39.5}Ni_{25}$ alloy, regardless of processing technique, a single-phase fcc matrix was observed with Al and Ni enrichment in the interdendritic regions, providing a chemical imprint with varying local chemical driving forces between intra- and interdendritic regions for B2-phase nucleation and growth. Subsequent aging treatments initiated site-specific phase transformation in ultra-fine interdendritic regions after the PBF-LB/M process. Thus, the potential to predetermine microstructures before post-processing, such as aging heat treatments, to induce the formation of secondary phases in specific locations within as-solidified microstructures was demonstrated.
- In the $Al_{14.5}Co_{25}Fe_{35.5}Ni_{25}$ alloy, the enrichment of Al and Ni in the liquid phase facilitated the stabilization of interdendritic B2-NiAl through segregation-mediated phase nucleation and growth, resulting in a dual-phase fcc/B2-NiAl matrix after complete solidification. Additionally, the thermal conditions during solidification effectively controlled the size, morphology and distribution of the interdendritic B2-NiAl phase.
- Multiphase-field simulations and experimental characterization demonstrated the flexible control of dendritic spacings and B2-NiAl -phase content through tuning the degree of undercooling driven by the cooling rate ($\dot{T}$) and solute trapping initiated by solidification velocities (R). The findings revealed that utilizing the PBF-LB/M process, e.g., increasing $\dot{T}$, could reduce dendritic spacings to a sub-micron scale, while almost two orders of magnitude larger dendrite spacings were observed for the alloys processed by ingot casting. Moreover, an increase in R and $\dot{T}$ also suppressed the area fraction and Al concentration of interdendritic regions, resulting in the lowest B2-NiAl-phase fraction for $Al_{14.5}Co_{25}Fe_{35.5}Ni_{25}$ alloy at the end of solidification during the PBF-LB/M process.
- Additionally, thermal histories associated with AM resulted in more pronounced structural heterogeneities. This modification was particularly severe in the case of PBF10.5 and PBF14.5 states, exhibiting the largest fraction of low-angle grain boundaries (LAGBs) and more heterogeneous in-grain local misorientation distribution. Consequently, refinement of primary dendrite arm spacings (PDAS) and corresponding microsegregation patterns were accompanied by an increase in structural heterogeneity of the microstructure, notably evident in the PBF-LB/M processed states.

Our approach aims at offering a perspective on utilizing as-solidified microstructures more effectively and can be achieved through the control of site-specific compositional and structural gradients via tailored solidification. From our perspective, AM brings an unmatched opportunity, especially PBF-LB/M with its very high cooling rates, as it results in fine microstructures and gives unique opportunities to locally modify the microstructure evolution due to its fashion of layer-wise fabrication and easily adaptable thermal conditions within confined melt-pools [5, 19]. However, coarser microstructures can also be designed depending on requirements, for instance, via casting methods. While our findings are applicable to alloys solidifying with one primary phase, we also anticipate that they can be extended to more complex materials experiencing solid-state phase transformations during solidification [5]. This extension would also enable the tailoring of microstructural features and the control of local phase transformations during or after solidification processes.

CRediT authorship contribution statement

Ahmet Turnali: Writing – review & editing, Writing – original draft, Visualization, Software, Methodology, Investigation, Formal analysis, Data curation, Conceptualization. **Dilay Kibaroglu:** Writing – review & editing, Visualization, Software, Formal analysis. **Nico Evers:** Investigation, Formal analysis. **Jaqueline Gehlmann:** Investigation. **Lennart Sayk:** Writing – review & editing, Investigation. **Nicolas J. Peter:** Investigation. **Abdelrahman Elsayed:** Investigation. **Mehdi Noori:** Software. **Tarek Allam:** Investigation. **Johannes Henrich Schleifenbaum:** Writing – review & editing, Resources. **Christian Haase:** Writing – review & editing, Supervision, Methodology, Funding acquisition, Conceptualization.

Declaration of competing interest

The authors declare that they have no known competing financial interests or personal relationships that could have appeared to influence the work reported in this paper.

Acknowledgements

This work has received funding from the German Federal Ministry of Education and Research (BMBF) as part of the NanoMatFutur project "MatAM - Design of additively manufactured high-performance alloys for automotive applications" (Project ID: 03XP0264) and from the European Research Council (ERC) under the European Union's Horizon Europe research and innovation program (grant agreement No. 101077977 HeteroGenius4D). This study includes results acquired from experiments conducted at the Ernst Ruska-Centre (ER-C) for Microscopy and Spectroscopy with Electrons at the Forschungszentrum Jülich (FZJ) in Germany [https://doi.org/10.17815/jlsrf-2–68, https://doi.org/10.17815/jlsrf-2–106]. Beamtime access to the ER-C was provided through the DFG Core Facility Project (FZJ_IEK2_PN1). The authors would like to acknowledge Deutsches Elektronen-Synchotron (DESY, Hamburg, Germany), a member Helmholtz Association HGF, for the allocation of experimental facilities. The SYXRD beamtime at DESY was allocated for proposal I-20220679 EC. The authors wish to thank Zoltan Hegedüs at DESY for the guidance with using beamline P21.2 at PETRA III and they also gratefully acknowledge the support of Eftyhmios Polatidis (University of Patras, Greece) and Christos Sofras (Paul Scherrer Institut, Switzerland) with the SYXRD measurements. The authors would also like to acknowledge the fruitful discussions on CALPHAD simulations with Bengt Hallstedt (RWTH Aachen University, Germany) and support of Jan-Philipp Roth (University of Applied Sciences Osnabrück, Germany) for atomization of the utilized $Al_{10.5}Co_{25}Fe_{39.5}Ni_{25}$ alloy powder.

Appendix A. Supplementary data

Supplementary data to this article can be found online at https://doi.org/10.1016/j.mtadv.2024.100549.

Data availability

Data will be made available on request.

References

[1] E.J. Pickering, Macrosegregation in steel ingots: the applicability of modelling and characterisation techniques, ISIJ Int. 53 (2013) 935–949, https://doi.org/10.2355/isijinternational.53.935.

[2] S. Kou, Welding Metallurgy, second ed., John Wiley & Sons, Hoboken, NJ, 2003.

[3] D. Raabe, M. Herbig, S. Sandlöbes, Y. Li, D. Tytko, M. Kuzmina, D. Ponge, P.-P. Choi, Grain boundary segregation engineering in metallic alloys: a pathway to the design of interfaces, Curr. Opin. Solid State Mater. Sci. 18 (2014) 253–261, https://doi.org/10.1016/j.cossms.2014.06.002.

[4] D. Raabe, D. Ponge, M.-M. Wang, M. Herbig, M. Belde, H. Springer, 1 billion tons of nanostructure – segregation engineering enables confined transformation effects at lattice defects in steels, IOP Conf. Ser. Mater. Sci. Eng. 219 (2017) 12006, https://doi.org/10.1088/1757-899X/219/1/012006.

[5] Ahmet Turnali, S. Amir H. Motaman, Yuling Chang, Bernd Böttger, Alexandros Serafeim, Lennart Sayk, Nicolas J. Peter, Silvia Richter, Alexander Schwedt, Simon Höges, Christian Haase, Evolution of microstructural heterogeneities in additively manufactured low-alloy steel, Addit. Manuf. 78 (2023) 103859, https://doi.org/10.1016/j.addma.2023.103859.

[6] Y. Zhao, Z. Ma, L. Yu, Y. Liu, New alloy design approach to inhibiting hot cracking in laser additive manufactured nickel-based superalloys, Acta Mater. 247 (2023) 118736, https://doi.org/10.1016/j.actamat.2023.118736.

[7] H. Yu, J. Fu, C. Wang, Y. Chen, L. Wang, H. Fang, J. Li, S. van der Zwaag, W. Xu, Robust additive manufacturable Ni superalloys designed by the integrated optimization of local elemental segregation and cracking susceptibility criteria, Acta Mater. 266 (2024) 119658, https://doi.org/10.1016/j.actamat.2024.119658.

[8] S. Thapliyal, P. Agrawal, P. Agrawal, S.S. Nene, R.S. Mishra, B.A. McWilliams, K. C. Cho, Segregation engineering of grain boundaries of a metastable Fe-Mn-Co-Cr-Si high entropy alloy with laser-powder bed fusion additive manufacturing, Acta Mater. 219 (2021) 117271, https://doi.org/10.1016/j.actamat.2021.117271.

[9] Z. Sun, X. Tan, C. Wang, M. Descoins, D. Mangelinck, S.B. Tor, E.A. Jägle, S. Zaefferer, D. Raabe, Reducing hot tearing by grain boundary segregation engineering in additive manufacturing: example of an AlxCoCrFeNi high-entropy alloy, Acta Mater. 204 (2021) 116505, https://doi.org/10.1016/j.actamat.2020.116505.

[10] Z. Sun, Y. Ma, D. Ponge, S. Zaefferer, E.A. Jägle, B. Gault, A.D. Rollett, D. Raabe, Thermodynamics-guided alloy and process design for additive manufacturing, Nat. Commun. 13 (2022) 4361, https://doi.org/10.1038/s41467-022-31969-y.

[11] J.M. Park, P. Asghari-Rad, A. Zargaran, J.W. Bae, J. Moon, H. Kwon, J. Choe, S. Yang, J.-H. Yu, H.S. Kim, Nano-scale heterogeneity-driven metastability engineering in ferrous medium-entropy alloy induced by additive manufacturing, Acta Mater. 221 (2021) 117426, https://doi.org/10.1016/j.actamat.2021.117426.

[12] F. Kies, P. Köhnen, M.B. Wilms, F. Brasche, K.G. Pradeep, A. Schwedt, S. Richter, A. Weisheit, J.H. Schleifenbaum, C. Haase, Design of high-manganese steels for additive manufacturing applications with energy-absorption functionality, Mater. Des. 160 (2018) 1250–1264, https://doi.org/10.1016/j.matdes.2018.10.051.

[13] P. Köhnen, S. Ewald, J.H. Schleifenbaum, A. Belyakov, C. Haase, Controlling microstructure and mechanical properties of additively manufactured high-strength steels by tailored solidification, Addit. Manuf. 35 (2020) 101389, https://doi.org/10.1016/j.addma.2020.101389.

[14] C. Kumara, A.R. Balachandramurthi, S. Goel, F. Hanning, J. Moverare, Toward a better understanding of phase transformations in additive manufacturing of Alloy 718, Materialia 13 (2020) 100862, https://doi.org/10.1016/j.mtla.2020.100862.

[15] C. Guo, S. Wei, Z. Wu, P. Wang, B. Zhang, U. Ramamurty, X. Qu, Effect of dual phase structure induced by chemical segregation on hot tearing reduction in additive manufacturing, Mater. Des. 228 (2023) 111847, https://doi.org/10.1016/j.matdes.2023.111847.

[16] Y. Chang, C. Haase, D. Szeliga, L. Madej, U. Hangen, M. Pietrzyk, W. Bleck, Compositional heterogeneity in multiphase steels: characterization and influence on local properties, Mater. Sci. Eng., A 827 (2021) 142078, https://doi.org/10.1016/j.msea.2021.142078.

[17] D. Kong, C. Dong, S. Wei, X. Ni, L. Zhang, R. Li, L. Wang, C. Man, X. Li, About metastable cellular structure in additively manufactured austenitic stainless steels, Addit. Manuf. 38 (2021) 101804, https://doi.org/10.1016/j.addma.2020.101804.

[18] Victor I. Tkatch, Alexander I. Limanovskii, Sergey N. Denisenko, Sergey G. Rassolov, The effect of the melt-spinning processing parameters on the rate of cooling, Mater. Sci. Eng., A 323 (2002) 91–96, https://doi.org/10.1016/S0921-5093(01)01346-6.

[19] S. Gao, Z. Li, S. van Petegem, J. Ge, S. Goel, J.V. Vas, V. Luzin, Z. Hu, H.L. Seet, D. F. Sanchez, H. van Swygenhoven, H. Gao, M. Seita, Additive manufacturing of alloys with programmable microstructure and properties, Nat. Commun. 14 (2023) 6752, https://doi.org/10.1038/s41467-023-42326-y.

[20] P. Köhnen, M. Létang, M. Voshage, J.H. Schleifenbaum, C. Haase, Understanding the process-microstructure correlations for tailoring the mechanical properties of L-PBF produced austenitic advanced high strength steel, Addit. Manuf. 30 (2019) 100914, https://doi.org/10.1016/j.addma.2019.100914.

[21] T. Allam, K.G. Pradeep, P. Köhnen, A. Marshal, J.H. Schleifenbaum, C. Haase, Tailoring the nanostructure of laser powder bed fusion additively manufactured maraging steel, Addit. Manuf. 36 (2020) 101561, https://doi.org/10.1016/j.addma.2020.101561.

[22] D. Raabe, S. Sandlöbes, J. Millán, D. Ponge, H. Assadi, M. Herbig, P.-P. Choi, Segregation engineering enables nanoscale martensite to austenite phase transformation at grain boundaries: a pathway to ductile martensite, Acta Mater. 61 (2013) 6132–6152, https://doi.org/10.1016/j.actamat.2013.06.055.

[23] D.B. Miracle, O.N. Senkov, A critical review of high entropy alloys and related concepts, Acta Mater. 122 (2017) 448–511, https://doi.org/10.1016/j.actamat.2016.08.081.

[24] F. Kies, Y. Ikeda, S. Ewald, J.H. Schleifenbaum, B. Hallstedt, F. Körmann, C. Haase, Combined Al and C alloying enables mechanism-oriented design of multi-principal element alloys: ab initio calculations and experiments, Scripta Mater. 178 (2020) 366–371, https://doi.org/10.1016/j.scriptamat.2019.12.004.

[25] E.P. George, W.A. Curtin, C.C. Tasan, High entropy alloys: a focused review of mechanical properties and deformation mechanisms, Acta Mater. 188 (2020) 435–474, https://doi.org/10.1016/j.actamat.2019.12.015.

[26] F. Wei, S. Wei, K.B. Lau, W.H. Teh, J.J. Lee, H.L. Seng, C.C. Tan, P. Wang, U. Ramamurty, Compositionally graded AlxCoCrFeNi high-entropy alloy manufactured by laser powder bed fusion, Materialia 21 (2022) 101308, https://doi.org/10.1016/j.mtla.2021.101308.

[27] T. Yang, S. Xia, S. Liu, C. Wang, S. Liu, Y. Zhang, J. Xue, S. Yan, Y. Wang, Effects of AL addition on microstructure and mechanical properties of Al CoCrFeNi High-entropy alloy, Mater. Sci. Eng., A 648 (2015) 15–22, https://doi.org/10.1016/j.msea.2015.09.034.

[28] K. Park, B. Cho, S.J. Hong, K.R. Lim, C. Lee, G. Song, Outstanding high-temperature strength of novel Fe–Cr–Ni–Al–V ferritic alloys with hierarchical B2–NiAl precipitates, Mater. Sci. Eng., A 840 (2022) 142999, https://doi.org/10.1016/j.msea.2022.142999.

[29] Raymond Kwesi Nutor, Qingping Cao, Ran Wei, Qingmei Su, Gaohui Du, Xiaodong Wang, Fushan Li, Dongxian Zhang, Jian-Zhong Jiang, A dual-phase alloy with ultrahigh strength-ductility synergy over a wide temperature range, Sci. Adv. 7 (2021) eabi4404, https://doi.org/10.1126/sciadv.abi4404.

[30] K.R. Lim, K.S. Lee, J.S. Lee, J.Y. Kim, H.J. Chang, Y.S. Na, Dual-phase high-entropy alloys for high-temperature structural applications, J. Alloys Compd. 728 (2017) 1235–1238, https://doi.org/10.1016/j.jallcom.2017.09.089.

[31] Y. Ma, J. Hao, Q. Wang, C. Zhang, C. Li, C. Dong, Temperature-affected microstructural stability of coherent cuboidal B2 particles in precipitation-strengthened body-centered-cubic Al0.7CoCr2FeNi high-entropy alloy, J. Mater. Sci. 54 (2019) 8696–8710, https://doi.org/10.1007/s10853-019-03459-y.

[32] P. Cui, Y. Liu, F. Zhou, Z. Lai, J. Zhu, Enhancing high temperature mechanical properties via modulating B2 phase with Al contents in FeCrNiAlx(x = 0.63,0.71,0.77) high entropy alloys, J. Alloys Compd. 903 (2022) 163883, https://doi.org/10.1016/j.jallcom.2022.163883.

[33] J.O. Andersson, Thomas Helander, Lars Höglund, Pingfang Shi, Bo Sundman, Thermo-Calc & DICTRA, computational tools for materials science, Calphad 26 (2002) 273–312, https://doi.org/10.1016/S0364-5916(02)00037-8.

[34] Bengt Hallstedt, Mehdi Noori, Fabian Kies, Felix Oppermann, Christian Haase, Thermodynamic database for multi-principal element alloys within the system Al–Co–Cr–Fe–Mn–Ni–C, Calphad 83 (2023) 102644, https://doi.org/10.1016/j.calphad.2023.102644.

[35] B. Böttger, J. Eiken, M. Apel, Multi-ternary extrapolation scheme for efficient coupling of thermodynamic data to a multi-phase-field model, Comput. Mater. Sci. 108 (2015) 283–292, https://doi.org/10.1016/j.commatsci.2015.03.003.

[36] J. Eiken, B. Böttger, I. Steinbach, Multiphase-field approach for multicomponent alloys with extrapolation scheme for numerical application, Phys. Rev. E: Stat., Nonlinear, Soft Matter Phys. 73 (2006) 66122, https://doi.org/10.1103/PhysRevE.73.066122.

[37] G. Boussinot, M. Döring, S. Hemes, O. Stryzhyboroda, M. Apel, M. Schmidt, Laser powder bed fusion of eutectic Al–Ni alloys: experimental and phase-field studies, Mater. Des. 198 (2021) 109299, https://doi.org/10.1016/j.matdes.2020.109299.

[38] T. DebRoy, H.L. Wei, J.S. Zuback, T. Mukherjee, J.W. Elmer, J.O. Milewski, A. M. Beese, A. Wilson-Heid, A. De, W. Zhang, Additive manufacturing of metallic components – process, structure and properties, Prog. Mater. Sci. 92 (2018) 112–224, https://doi.org/10.1016/j.pmatsci.2017.10.001.

[39] D. Herzog, V. Seyda, E. Wycisk, C. Emmelmann, Additive manufacturing of metals, Acta Mater. 117 (2016) 371–392, https://doi.org/10.1016/j.actamat.2016.07.019.

[40] B. Böttger, M. Apel, Phase-field simulation of the formation of new grains by fragmentation during melting of an ABD900 superalloy, IOP Conf. Ser. Mater. Sci. Eng. 1281 (2023) 12008, https://doi.org/10.1088/1757-899X/1281/1/012008.

[41] A. Carré, B. Böttger, M. Apel, Implementation of an antitrapping current for a multicomponent multiphase-field ansatz, J. Cryst. Growth 380 (2013) 5–13, https://doi.org/10.1016/j.jcrysgro.2013.05.032.

[42] C.A. Schneider, W.S. Rasband, K.W. Eliceiri, NIH Image to ImageJ: 25 years of image analysis, Nat. Methods 9 (2012) 671–675, https://doi.org/10.1038/nmeth.2089.

[43] F. Bachmann, R. Hielscher, H. Schaeben, Texture analysis with MTEX – free and open source software toolbox, SSP 160 (2010) 63–68. https://doi.org/10.4028/www.scientific.net/SSP.160.63.

[44] F. Bachmann, R. Hielscher, H. Schaeben, Grain detection from 2d and 3d EBSD data–specification of the MTEX algorithm, Ultramicroscopy 111 (2011) 1720–1733, https://doi.org/10.1016/j.ultramic.2011.08.002.

[45] G. Nolze, R. Hielscher, Orientations – perfectly colored, J. Appl. Crystallogr. 49 (2016) 1786–1802, https://doi.org/10.1107/S1600576716012942.

[46] M.N. Gussev, K.J. Leonard, In situ SEM-EBSD analysis of plastic deformation mechanisms in neutron-irradiated austenitic steel, J. Nucl. Mater. 517 (2019) 45–56, https://doi.org/10.1016/j.jnucmat.2019.01.034.

[47] W. Kurz, D. Fisher, Fundamentals of Solidification, Trans Tech Publications Limited, 1998.

[48] R. Trivedi, W. Kurz, Solidification microstructures: a conceptual approach, Acta Metall. Mater. 42 (1994) 15–23, https://doi.org/10.1016/0956-7151(94)90044-2.

[49] P.K. Galenko, E.V. Abramova, D. Jou, D.A. Danilov, V.G. Lebedev, D.M. Herlach, Solute trapping in rapid solidification of a binary dilute system: a phase-field study,

Phys. Rev. E: Stat., Nonlinear, Soft Matter Phys. 84 (2011) 41143, https://doi.org/10.1103/PhysRevE.84.041143.
[50] S. Ghosh, L. Ma, N. Ofori-Opoku, J.E. Guyer, On the primary spacing and microsegregation of cellular dendrites in laser deposited Ni-Nb alloys, Model. Simulat. Mater. Sci. Eng. 25 (2017), https://doi.org/10.1088/1361-651x/aa7369.
[51] S. Ghosh, J. Zollinger, M. Zaloznik, D. Banerjee, C.K. Newman, R. Arroyave, Modeling of hierarchical solidification microstructures in metal additive manufacturing: challenges and opportunities, Addit. Manuf. 78 (2023) 103845, https://doi.org/10.1016/j.addma.2023.103845.
[52] G. Wang, H. Ouyang, C. Fan, Q. Guo, Z. Li, W. Yan, Z. Li, The origin of high-density dislocations in additively manufactured metals, Materials Research Letters 8 (2020) 283–290, https://doi.org/10.1080/21663831.2020.1751739.
[53] S. Gao, Z. Hu, M. Duchamp, P.S.R. Krishnan, S. Tekumalla, X. Song, M. Seita, Recrystallization-based grain boundary engineering of 316L stainless steel produced via selective laser melting, Acta Mater. 200 (2020) 366–377, https://doi.org/10.1016/j.actamat.2020.09.015.
[54] Y.M. Wang, T. Voisin, J.T. McKeown, J. Ye, N.P. Calta, Z. Li, Z. Zeng, Y. Zhang, W. Chen, T.T. Roehling, R.T. Ott, M.K. Santala, P.J. Depond, M.J. Matthews, A. V. Hamza, T. Zhu, Additively manufactured hierarchical stainless steels with high strength and ductility, Nat. Mater. 17 (2018) 63–71, https://doi.org/10.1038/nmat5021.
[55] Y. Hong, C. Zhou, Y. Zheng, L. Zhang, J. Zheng, X. Chen, B. An, Formation of strain-induced martensite in selective laser melting austenitic stainless steel, Mater. Sci. Eng., A 740–741 (2019) 420–426, https://doi.org/10.1016/j.msea.2018.10.121.
[56] H.E. Sabzi, E. Hernandez-Nava, X.-H. Li, H. Fu, D. San-Martín, P.E. Rivera-Díaz-del-Castillo, Strengthening control in laser powder bed fusion of austenitic stainless steels via grain boundary engineering, Mater. Des. 212 (2021) 110246, https://doi.org/10.1016/j.matdes.2021.110246.
[57] M.V. Pantawane, Y.-H. Ho, S.S. Joshi, N.B. Dahotre, Computational assessment of thermokinetics and associated microstructural evolution in laser powder bed fusion manufacturing of Ti6Al4V alloy, Sci. Rep. 10 (2020) 7579, https://doi.org/10.1038/s41598-020-63281-4.
[58] S.A. Khairallah, A.T. Anderson, A. Rubenchik, W.E. King, Laser powder-bed fusion additive manufacturing: physics of complex melt flow and formation mechanisms of pores, spatter, and denudation zones, Acta Mater. 108 (2016) 36–45, https://doi.org/10.1016/j.actamat.2016.02.014.
[59] X. Wu, Y. Zhu, Heterogeneous materials: a new class of materials with unprecedented mechanical properties, Materials Research Letters 5 (2017) 527–532, https://doi.org/10.1080/21663831.2017.1343208.
[60] Y. Zhu, X. Wu, Heterostructured materials, Prog. Mater. Sci. 131 (2023) 101019, https://doi.org/10.1016/j.pmatsci.2022.101019.
[61] E. DelVecchio, T. Liu, Y.-T. Chang, Y. Nie, M. Eslami, M.A. Charpagne, Metastable cellular structures govern localized corrosion damage development in additive manufactured stainless steel, npj Mater. Degrad. 8 (2024), https://doi.org/10.1038/s41529-024-00464-8.
[62] M. Tian, J.D. Choundraj, T. Voisin, Y.M. Wang, J. Kacher, Discovering the nanoscale origins of localized corrosion in additive manufactured stainless steel 316L by liquid cell transmission electron microscopy, Corrosion Sci. 208 (2022) 110659, https://doi.org/10.1016/j.corsci.2022.110659.
[63] R.I. Revilla, M. van Calster, M. Raes, G. Arroud, F. Andreatta, L. Pyl, P. Guillaume, I. de Graeve, Microstructure and corrosion behavior of 316L stainless steel prepared using different additive manufacturing methods: a comparative study bringing insights into the impact of microstructure on their passivity, Corrosion Sci. 176 (2020) 108914, https://doi.org/10.1016/j.corsci.2020.108914.
[64] J. Yao, Q. Tan, J. Venezuela, A. Atrens, M.-X. Zhang, Recent research progress in hydrogen embrittlement of additively manufactured metals – a review, Curr. Opin. Solid State Mater. Sci. 27 (2023) 101106, https://doi.org/10.1016/j.cossms.2023.101106.
[65] K. Büßenschütt, P. Köhnen, F. Kies, S. Koß, J.H. Schleifenbaum, C. Haase, High-speed direct energy deposition as a high-throughput design tool for laser-based additive manufacturing, Additive Manufacturing Letters 8 (2024) 100188, https://doi.org/10.1016/j.addlet.2023.100188.